

VALIDATION OF TWELVE SMALL *KEPLER* TRANSITING PLANETS IN THE HABITABLE ZONE

GUILLERMO TORRES^{1,2}, DAVID M. KIPPING¹, FRANCOIS FRESSIN¹, DOUGLAS A. CALDWELL³, JOSEPH D. TWICKEN³, SARAH BALLARD^{4,5}, NATALIE M. BATALHA⁶, STEPHEN T. BRYSON⁶, DAVID R. CIARDI⁷, CHRISTOPHER E. HENZE⁶, STEVE B. HOWELL⁶, HOWARD T. ISAACSON⁸, JON M. JENKINS⁶, PHILIP S. MUIRHEAD^{9,10}, ELISABETH R. NEWTON¹, ERIK A. PETIGURA⁸, THOMAS BARCLAY⁶, WILLIAM J. BORUCKI⁶, JUSTIN R. CREPP¹¹, MARK E. EVERETT¹², ELLIOTT P. HORCH¹³, ANDREW W. HOWARD¹⁴, REA KOLBL⁸, GEOFFREY W. MARCY⁸, SEAN MCCAULIFF¹⁵, AND ELISA V. QUINTANA⁶

To appear in The Astrophysical Journal

ABSTRACT

We present an investigation of twelve candidate transiting planets from *Kepler* with orbital periods ranging from 34 to 207 days, selected from initial indications that they are small and potentially in the habitable zone (HZ) of their parent stars. Few of these objects are known. The expected Doppler signals are too small to confirm them by demonstrating that their masses are in the planetary regime. Here we verify their planetary nature by validating them statistically using the BLENDER technique, which simulates large numbers of false positives and compares the resulting light curves with the *Kepler* photometry. This analysis was supplemented with new follow-up observations (high-resolution optical and near-infrared spectroscopy, adaptive optics imaging, and speckle interferometry), as well as an analysis of the flux centroids. For eleven of them (KOI-0571.05, 1422.04, 1422.05, 2529.02, 3255.01, 3284.01, 4005.01, 4087.01, 4622.01, 4742.01, and 4745.01) we show that the likelihood they are true planets is far greater than that of a false positive, to a confidence level of 99.73% (3σ) or higher. For KOI-4427.01 the confidence level is about 99.2% (2.6σ). With our accurate characterization of the GKM host stars, the derived planetary radii range from 1.1 to $2.7 R_{\oplus}$. All twelve objects are confirmed to be in the HZ, and nine are small enough to be rocky. Excluding three of them that have been previously validated by others, our study doubles the number of known rocky planets in the HZ. KOI-3284.01 (Kepler-438 b) and KOI-4742.01 (Kepler-442 b) are the planets most similar to the Earth discovered to date when considering their size and incident flux jointly.

Subject headings: methods: statistical — planetary systems — stars: individual (KOI-0571 = Kepler-186, KOI-1422 = Kepler-296, KOI-2529 = Kepler-436, KOI-3255 = Kepler-437, KOI-3284 = Kepler-438, KOI-4005 = Kepler-439, KOI-4087 = Kepler-440, KOI-4427, KOI-4622 = Kepler-441, KOI-4742 = Kepler-442, KOI-4745 = Kepler-443) — techniques: photometric

1. INTRODUCTION

Over the duration of its four-year mission the *Kepler* spacecraft has enabled the identification of several thousand candidate transiting planets (*Kepler* Objects of Interest, or KOIs; Borucki et al. 2011; Batalha et al. 2013; Burke et al. 2014), and many more continue to be found

from reanalysis of the original data with increasingly sophisticated methods. Only a tiny fraction of these candidates have been “confirmed” in the traditional sense of having had their masses measured, either spectroscopically or by modeling their transit timing variations (TTVs). Hundreds of others, mostly in multiple systems (“multis”), have recently been shown statistically to have a very high chance of being true planets (Lissauer et al. 2014; Rowe et al. 2014), even if their masses are not currently known.

Public curiosity and scientific interest have motivated efforts in the last few years to find and confirm rocky planets similar in size to the Earth that are orbiting in the so-called habitable zone (HZ) of their parent stars, usually taken in this context to be the region in which water on the surface can be in a liquid state. Recent estimates by Petigura et al. (2013) suggest the rate of occurrence of Earth-size planets in the HZ of Sun-like stars (which they defined broadly as corresponding to an incident flux between $\frac{1}{4}$ and 4 times that of the Earth) may be as high as $22 \pm 8\%$ (for other estimates see Zsom et al. 2013; Pintr et al. 2014; Foreman-Mackey et al. 2014), but very few of these have actually been confirmed. These two conditions for habitability — rocky nature and suitable location — are sometimes more challenging to establish unambiguously than it may seem, as they

¹ Harvard-Smithsonian Center for Astrophysics, 60 Garden Street, Cambridge, MA 02138, USA

² E-mail: gtorres@cfa.harvard.edu

³ SETI Institute/NASA Ames Research Center, Moffett Field, CA 94035, USA

⁴ University of Washington, Seattle, WA 98195, USA

⁵ NASA Carl Sagan Fellow

⁶ NASA Ames Research Center, Moffett Field, CA 94035, USA

⁷ NASA Exoplanet Science Institute/Caltech, Pasadena, CA 91125, USA

⁸ Astronomy Department, University of California, Berkeley, CA 94720, USA

⁹ Department of Astronomy, Boston University, Boston, MA 02215, USA

¹⁰ Hubble Postdoctoral Fellow

¹¹ University of Notre Dame, Notre Dame, IN 46556, USA

¹² National Optical Astronomy Observatory, Tucson, AZ 85719, USA

¹³ Department of Physics, Southern Connecticut State University, New Haven, CT 06515, USA

¹⁴ Institute for Astronomy, University of Hawaii at Manoa, Honolulu, HI 96822, USA

¹⁵ Orbital Sciences Corporation/NASA Ames Research Center, Moffett Field, CA 94035, USA

require an accurate knowledge of the host star properties, something that is not always trivial to achieve for the faint *Kepler* targets. Definitions of the HZ are actively debated and have changed over time (e.g., Kasting et al. 1993; Selsis et al. 2007; Kopparapu et al. 2013; Seager 2013; Leconte et al. 2013; Zsom et al. 2013; Kopparapu et al. 2014), as has our understanding of the radius at which planets transition from being rocky to being dominated by thick hydrogen/helium envelopes, which presumably makes them unsuitable for life as we know it. The interface is currently thought to be between 1.5 and $2 R_{\oplus}$ (e.g., Lopez & Fortney 2013; Weiss & Marcy 2014; Marcy et al. 2014; Rogers 2014; Wolfgang & Lopez 2014), but many uncertainties remain and it is possible that some planets that are slightly larger may still be rocky.

These difficulties notwithstanding, a handful of transiting planets that appear to meet these conditions have already emerged from the *Kepler* sample. Among those considered at the time of publication to be smaller than $2.5 R_{\oplus}$ and in or near the HZ, the first to be announced was Kepler-22b (Borucki et al. 2012), with a radius of $R_p = 2.38 \pm 0.13 R_{\oplus}$. Others followed including Kepler-61b ($2.15 \pm 0.13 R_{\oplus}$; Ballard et al. 2013), Kepler-62e and f ($1.61 \pm 0.05 R_{\oplus}$ and $1.41 \pm 0.07 R_{\oplus}$; Borucki et al. 2013), Kepler-69c ($1.71^{+0.34}_{-0.23} R_{\oplus}$; Barclay et al. 2013), and recently Kepler-186f ($1.11 \pm 0.14 R_{\oplus}$; Quintana et al. 2014). All of these were “validated” statistically using techniques such as BLENDER (Torres et al. 2004, 2011; Fressin et al. 2012) by examining the likelihood of different false positive scenarios to measure the confidence in the planetary interpretation. Some of them are in multi-planet systems; as mentioned above, Lissauer et al. (2014) have developed a statistical argument by which they demonstrate that most candidates in multis are very likely to be true planets. Based on this reasoning and a careful examination of follow-up observations, Lissauer et al. (2014) reported an additional small planet (Kepler-296f, $2.31 \pm 0.12 R_{\oplus}$) that appears to be in the HZ, according to Rowe et al. (2014). Taking advantage of the same statistical framework for validation, the latter authors announced one more small HZ planet in a multi-planet system: Kepler-174d ($2.19 \pm 0.13 R_{\oplus}$). Other small HZ candidates have been proposed (see, e.g., Muirhead et al. 2012; Dressing & Charbonneau 2013; Gaidos 2013; Mann et al. 2013b; Petigura et al. 2013; Star et al. 2014) but have yet to be investigated in detail and confirmed. A few additional examples also believed to be in this special group were later shown to fail one or both requirements (size and location), either because of incorrect stellar parameters (originally based on photometry and later improved with spectroscopy) or because of the discovery of other stars in the photometric aperture that dilute the transits and change the inferred planetary radius (e.g., Star et al. 2014).

In this paper we investigate a sample of twelve *Kepler* candidates identified on the basis of preliminary analyses indicating that they are small and likely to be in or near the HZ of their parent stars. Our goal is to validate them as bona-fide planets, and to confirm their key properties pertaining to habitability. We describe our efforts over the past year to obtain the follow-up observations necessary to robustly characterize the host

stars and to validate the signals. In the interim, three of them that are in systems with five candidates each (KOI-0571.05 = Kepler-186f, KOI-1422.04 = Kepler-296f, and KOI-1422.05 = Kepler-296e) were the subject of recent studies by others. KOI-1422.04 and KOI-1422.05 were announced as planets by Lissauer et al. (2014) and Rowe et al. (2014) using their statistical framework for validation of multis “in bulk”, though only the first was mentioned as being in the HZ. KOI-0571.05 was validated independently by Quintana et al. (2014). These authors relied in part on the fact that false positives are much less common in multis, and on the validation of the other four planets in the same system by the previous authors, in order to reach a sufficiently high level of confidence for the fifth candidate. Most of the other targets in our sample are considerably more difficult to validate because they tend to have long orbital periods and do not belong to multiple systems. Nevertheless, as we show below, the application of the BLENDER technique used in many of the previous discoveries is able to achieve validations here as well. Our work has now essentially doubled the number of known small HZ planets.

Our paper is organized as follows: Sect. 2 and Sect. 3 describe our sample of candidates and the *Kepler* photometry we use. The follow-up observations including high-resolution imaging, optical spectroscopy, and near-infrared spectroscopy are presented in Sect. 4, where we also report the complicating discovery of nearby stellar companions to four of the targets. These close companions not only dilute the transits but also bring ambiguity as to the precise location of the planets in these systems. A description of the analysis of the flux centroids that addresses some of those companions is given here as well. Sect. 5 follows with a determination of the stellar properties. The formal validation of our candidates is the subject of Sect. 6, after which we proceed with the transit light curve fits to derive the planetary parameters (Sect. 7). In Sect. 8 we apply the powerful technique of asteroid density profiling to investigate whether the planets that are in multiple systems orbit the same star, to extract eccentricity information from the light curves of our targets, and for the four host stars with close stellar companions, to address the possibility that the planets orbit the companions rather than the intended targets. The topic of habitability is examined in Sect. 9. We conclude with a discussion of our findings and final remarks.

2. CANDIDATE IDENTIFICATION

Candidate transiting planets of special interest for this study were initially identified as ‘threshold crossing events’ (TCEs; objects with a 7.1σ or greater multiple-event transit detection statistic; see Jenkins et al. 2002, 2010) from a transit search conducted using nearly three years of *Kepler* data gathered from quarters 1 to 12, with version 8.3 of the Science Operations Center (SOC) processing pipeline (Tenenbaum et al. 2013). The analysis of three years of data gave us the first chance to detect three transits from planets in habitable-zone orbits around stars like the Sun, as well as to significantly increase the signal-to-noise ratio (SNR) for transit signals from habitable-zone orbits around cooler stars. In order to investigate the smaller planets potentially in the HZ, we selected for further scrutiny the TCEs that met the criteria $R_p < 2 R_{\oplus}$ and $T_{\text{eq}} < 303$ K, as well as a transit

SNR > 7 . Here T_{eq} represents the planetary equilibrium temperature, calculated assuming an Earth-like albedo, and the stellar properties relied on information from the *Kepler* Input Catalog (KIC; Brown et al. 2011). We used data products from versions 8.3 and 9.0 of the SOC Data Validation (DV) pipeline module for the initial triage and vetting (for an overview of this process, see Wu et al. 2010)¹⁶. We compared the results of our vetting with the scores from early runs of an automated vetting code being developed at the time (McCauliff et al. 2014). From the 18,407 TCEs that passed through DV, we identified 385 TCEs around 338 unique stars that met our selection criteria. From this list of 385 TCEs we identified ten that passed flux and centroid vetting criteria and that had low false-alarm probabilities from the auto-vetter. During this vetting process, the SOC completed a transit search of *Kepler* data from quarters 1–16 using version 9.1 of the processing pipeline. With the addition of three quarters of data and the improvements in the version 9.1 DV products, we promoted an additional TCE (KOI-4742.01), which had marginal signal-to-noise ratio in the 12-quarter run, and identified KOI-1422.05, the fifth KOI and second habitable-zone candidate around this star. The complete list of targets selected for this study is given in Table 1.

We note that there is significant contamination of the TCE list for periods near the orbital period of the *Kepler* spacecraft (372 days) caused by instrumental image artifacts on specific detector channels, as has been noted by Tenenbaum et al. (2013). The contamination is due to moiré pattern noise injected during readout of some of the detector chains (Caldwell et al. 2010; Kolodziejczak et al. 2010). The moiré noise generates a host of single-event transit-like signals for targets on the noisy channel. When folded at a period near one *Kepler* year these signals can give multiple-event statistics above the 7.1σ detection threshold, as the same target star falls on the same noisy channel. We have not included any KOIs from the moiré pattern noise channels in our analysis here. Two of the KOIs (KOI-2529.02 and KOI-4005.01) do show some of their transits on detector channel 56, which has increased noise relative to the other channels on which these targets fall. However, we included these KOIs in our sample because both show transits on other channels and both passed all of our vetting checks.

3. KEPLER PHOTOMETRY

For the analysis in this paper we have made use of the publicly available *Kepler* data for each KOI from the Mikulski Archive for Space Telescopes (MAST).¹⁷ The observations span *Kepler* quarters 1–17, corresponding to a period of four years beginning in 2009 May. The downloaded data were made available as part of Data Release 23 and were processed using SOC Pipeline version 9.1. While long-cadence (29.4 min) data were available for all KOIs, short-cadence (58.9 s) data were only available for KOI-0571 and KOI-1422. In the following we describe our further processing of the simple aperture photometry (SAP) time series used for the detailed light-curve

analysis of all KOIs. Later in Sect. 5.1 and Sect. 6.1 we describe the slightly different processing of the photometry used to extract stellar rotation information and for the BLENDER analysis.

Prior to making use of the SAP measurements we removed instrumental and stellar photometric variability in the *Kepler* data that can disturb the transit light curve profile. This process was conducted in two steps: pre-detrending cleaning, and long-term detrending. The pre-detrending cleaning was carried out independently for each transit event, restricted to plus or minus half an orbital period surrounding the mid-transit time. We visually inspected each epoch and removed any charge-trapping ramps, flare-like events, and instrumental discontinuities in the data. We made no attempt to correct these artifacts and simply excluded them from the photometry manually. We then removed all of the transit signals of the other known candidates in each system (for stars having multiple candidates) within ± 0.6 transit durations centered on the mid-times, using the reported ephemerides. Finally, we cleaned the data of 3σ outliers from a moving median smoothing curve with a 20-point window.

Next we removed long-term trends, which can be due to instrumental effects such as focus drift, or stellar effects such as rotational modulations. For this task we used the Cosine Filtering with Autocorrelation Minimization (CoFiAM) algorithm, which was specifically developed to protect the shape of a transit light curve. We briefly highlight the main features of CoFiAM and the specific inputs used for this analysis, and we direct the reader to Kipping et al. (2013) for a more detailed description of the technique. It is essentially a Fourier-based method that removes periodicities occurring at timescales greater than a pre-designated “protected timescale”. In this work, we selected three times the known transit duration to be the protected timescale, which ensures that the transit profile is not distorted in frequency space. CoFiAM does not directly attempt to remove high frequency noise, since the Fourier transform of a trapezoidal-like light curve contains significant high frequency power (Waldmann 2012). It is able to explore many different harmonics by trying longer protected timescales than the nominal choice (we capped the maximum number of harmonics at 30) and evaluate the autocorrelation at a pre-selected timescale (we used 30 minutes) locally surrounding each transit. From these different harmonics, we selected the harmonic order that minimizes this local autocorrelation, as quantified using the Durbin-Watson statistic. This “Autocorrelation Minimization” component of CoFiAM provides optimized data for subsequent analysis. For each KOI we defined the local transit data as being within six transit durations either side of the mid-transit time, in order to provide an ample out-of-transit baseline. These local data were divided through by the final CoFiAM function and then stitched together to form our final light curve for analysis.

4. FOLLOW-UP OBSERVATIONS AND CENTROID ANALYSIS

4.1. High-resolution imaging

The presence of other stars blended with our targets is a potential concern, as these companions could be or-

¹⁶ All DV results are available from the NASA Exoplanet Archive: <http://exoplanetarchive.ipac.caltech.edu>.

¹⁷ <https://archive.stsci.edu/index.html>.

Table 1
Sample of KOIs in this study.

Candidate	Name	KID	Kp (mag)	b (deg)	Period (days)	Depth (ppm)
KOI-0571.05	Kepler-186 f	8120608	14.625	8.2	129.94	540
KOI-1422.04	Kepler-296 f	11497958	15.921	18.0	63.34	1070
KOI-1422.05	Kepler-296 e	11497958	15.921	18.0	34.14	850
KOI-2529.02	Kepler-436 b	8463346	15.856	6.5	64.00	1150
KOI-3255.01	Kepler-437 b	8183288	14.352	9.0	66.65	520
KOI-3284.01	Kepler-438 b	6497146	14.467	18.6	35.23	400
KOI-4005.01	Kepler-439 b	8142787	14.560	19.9	178.14	700
KOI-4087.01	Kepler-440 b	6106282	15.134	15.8	101.11	1010
KOI-4427.01		4172805	15.645	8.2	147.66	1220
KOI-4622.01	Kepler-441 b	11284772	15.142	19.1	207.25	960
KOI-4742.01	Kepler-442 b	4138008	14.976	15.0	112.31	560
KOI-4745.01	Kepler-443 b	11757451	15.891	17.0	177.67	930

Note. — Columns after the first indicate the *Kepler* planet designation, *Kepler* identification number, brightness in the *Kepler* passband, Galactic latitude, orbital period, and transit depth in parts per million relative to the out-of-transit stellar flux. For consistency in this paper we will refer to all objects by their original KOI names throughout, even though the validations described later earn them the official *Kepler* planet designations listed in the second column.

bited by another object causing eclipses that may be the source of the transit signals we observe. Even if they are not eclipsing, the light of the companion stars will attenuate the signal and lead to a bias in the planetary radius determination if the effect is not accounted for.

Images from the *J*-band UK Infrared Telescope survey (UKIRT; Lawrence et al. 2007) have indeed revealed companions to three of our targets (KOI-2529, 3284, and 4427) that are close enough to fall within the photometric aperture of *Kepler* (i.e., within a few arc seconds), although as we describe later they are ruled out as the source of the transits by our centroid analysis in Sect. 4.2. We list these companions in Table 2, based on information taken from the *Kepler* Community Follow-up Observing Program (CFOP) Web site¹⁸. Additional companions to three other KOIs are seen in the UKIRT images at larger separations (and are also excluded by the centroid analysis), but these stars are all very faint ($\Delta m \gtrsim 5$), and have a negligible impact on the inferred planetary sizes.

The UKIRT images have a typical seeing-limited resolution of about $0''.8$ or $0''.9$. To explore the inner regions around our targets beyond the reach of UKIRT we observed them with near-infrared adaptive optics (AO) in the *J* ($1.248 \mu\text{m}$) and *K'* ($2.124 \mu\text{m}$) filters using the NIRC2 imager (Wizinowich et al. 2004; Johansson et al. 2008) on the KeckII, 10 m telescope. KOI-0571 and KOI-3255 were observed in August 2012, and the rest in August 2013 as part of a general infrared AO survey of KOIs (e.g., Adams et al. 2012; Rowe et al. 2014; Marcy et al. 2014). KOI-1422 was not observed with AO for this project as it has been the target of a separate effort using *HST* (Gilliland et al. 2015; Star et al. 2014); those authors found it to have a close companion (see below). For KOI-0571, 3255, 2529, 3284, and 4742 the targets themselves were used as natural guide stars; for KOI-4005, 4087, 4427, 4622, and 4745 we used the laser guide-star AO system. In all cases the observations were obtained in a 3-point dither pattern to avoid the lower left quadrant of the NIRC2 array, which displays elevated

Table 2
Close companions to target stars.

Star	Ang. sep. ($''$)	P.A. (deg)	Mag. diff. ^a (mag)	Source
KOI-1422	0.220	216.3	$\Delta R = 1.72^b$	Speckle
KOI-2529	0.402	350.4	$\Delta K' = 4.69$	Keck AO
...	5.05	42.6	$\Delta J = 3.75$	UKIRT
KOI-3255	0.180 ^c	336.5	$\Delta K' = 0.05$	Keck AO
KOI-3284	0.438 ^c	193.2	$\Delta K' = 2.03$	Keck AO
...	4.10 ^d	359.7	$\Delta J = 2.90$	UKIRT
KOI-4427	4.76	274.8	$\Delta J = 2.87$	UKIRT

^a For targets with both a close and a wide companion the magnitude differences for the wide companions are relative to the total brightness of the inner pair.

^b Also observed at 880 nm (approximately Sloan *z* band), giving $\Delta z = 1.62$. The separation and P.A. in the table are the average of the two speckle bands. Similar results were reported by Star et al. (2014) from *HST* observations.

^c This companion was also detected in our speckle imaging observations.

^d This companion was also detected in the *UBV* survey of Everett et al. (2012), with magnitude differences $\Delta B = 1.80$ and $\Delta V = 2.01$. The separation and P.A. in the table are the average of the two surveys.

noise. Five images were collected per dither pattern position, each shifted $0''.5$ from the previous dither position to enable the use of the source frames for the creation of the sky image.

In general the NIRC2 imaging detects all of the sources found in the UKIRT *J*-band imaging within $5''$ of each target. The NIRC2 array has 1024×1024 pixels with a scale of about 10 mas pix^{-1} , and a field of view of $10''.1 \times 10''.1$. Each frame was dark-subtracted and flat-fielded, and the sky frames were constructed for each target from the target frames themselves by median filtering and co-adding the 15 or 25 dithered frames. Individual exposure times varied depending on the brightness of the target, but were long enough to obtain at least 5000 counts per frame (NIRC2 has a gain of 4 electrons per DN); frame times were typically 1–30 seconds. Data reduction was performed with a custom set of IDL routines. Close companions were detected around KOI-2529, 3255, and 3284 (see Figure 1), two of which also

¹⁸ <https://cfop.ipac.caltech.edu/home/>.

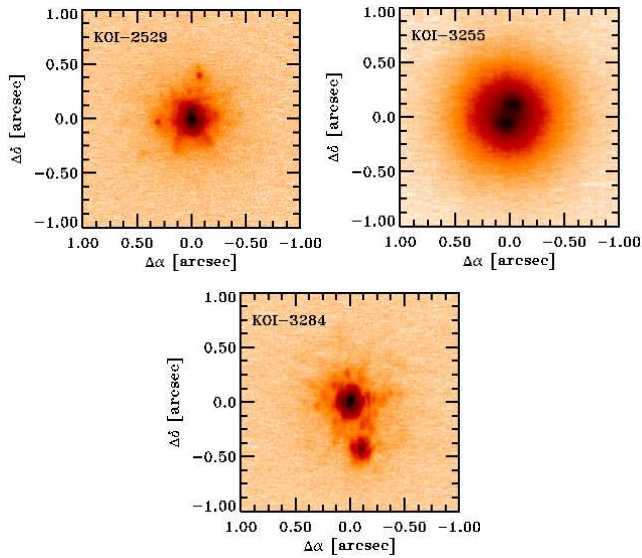


Figure 1. Images in the K' band from our Keck AO imaging observations showing close companions found around KOI-2529, KOI-3255, and KOI-3284 (see also Table 2).

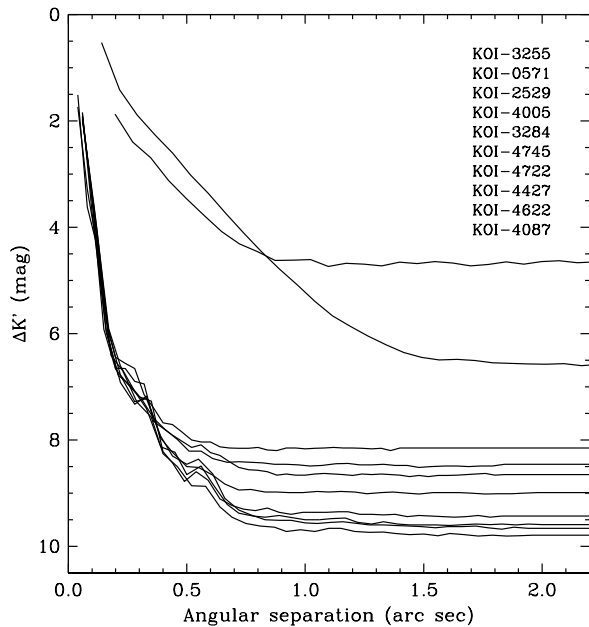


Figure 2. Sensitivity curves from our Keck AO imaging observations in the ($2.124\ \mu\text{m}$) K' band. Curves correspond to the KOIs as labeled, top to bottom.

have wider companions seen in the UKIRT images. We report the relative positions and brightness of these close companions also in Table 2.

Point source detection limits were estimated in a series of concentric annuli drawn around each target star. The separation and widths of the annuli were set to the full width at half maximum (FWHM) of the target point spread function (PSF). The standard deviation of the background counts was calculated for each annulus, and the 5σ limits were determined for each annular region (see also Adams et al. 2012). The PSF widths for our Keck images were typically found to be 4–5 pixels, corresponding to $0''.04$ – $0''.05$ FWHM. Typical contrast levels from the images are 2–3 magnitudes at a separation of 1

FWHM, 7–8 magnitudes at 5+ FWHM, and deeper past 10 FWHM. Sensitivity curves in the K' band for each of the targets are shown in Figure 2, and extend to angular separations of approximately $3''$, set by the dither pattern overlap. We supplemented these measurements with similar sensitivity estimates made from the UKIRT images available on the CFOP Web site, which reach to much wider separations but are not as deep.

Additional high-resolution imaging observations for four of our targets (KOI-0571, 1422, 3255, and 3284) were obtained with the Differential Speckle Survey Instrument (DSST; Horch et al. 2009; Howell et al. 2011) mounted on the 8.1m Gemini-N telescope during the time period UT 2012 July 25–28. The seeing conditions were generally $0''.5$ – $0''.8$ during those nights. The large aperture of the Gemini-N primary mirror allows for high SNR observations at faint magnitudes and achieves a very small diffraction limit for visible-light observations. The speckle camera provides simultaneous observations in two filters. For all Gemini-N observations discussed here we used filters centered at 692 nm and 880 nm (corresponding very roughly to the Cousins R and Sloan z bands), with band widths of 40 nm and 50 nm, respectively. Although full details of the observing protocols have been given previously by Horch et al. (2012), we summarize them here for completeness.

For bright targets observed with this instrument ($V < 12$) a single sequence of 1000 speckle frames of 60 ms duration each has usually been found to be sufficient, for a total of 3–4 minutes of observing time. The much fainter sources discussed here ($15 < V < 17$) required up to eight, 1000-frame sequences that were later combined, or about 30 minutes of on-source exposure time each. Calibration images and sequences were taken as is usual to allow us to measure and define dispersion effects, position angles, faint limit sensitivity, photometric performance, and for point source reconstruction.

The speckle observations revealed no stars in the vicinity of KOI-0571, but KOI-1422 was found to have a close companion (seen in both filters) that was also subsequently detected in the *HST* observations by Gilliland et al. (2015). Its brightness and position relative to the primary are given in Table 2. Close companions were also found around KOI-3255 and KOI-3284, which are the same as detected in our AO imaging with Keck.

For estimating our detection threshold for faint companions we considered each local maximum in the reconstructed image as a potential stellar source, and determined the statistics of these peaks (i.e., their average values and standard deviation) as a function of angular distance from the primary star. We then adopted a conservative 5σ threshold for the detection of any companion stars. The details of the calibration procedures mentioned above and the precision that may be obtained are described by Horch et al. (2011, 2012). The sensitivity curves for the four *Kepler* targets observed here with speckle imaging are shown in Figure 3.

4.2. Centroid analysis

One method to identify possible false positives due to background eclipsing binaries measures the location of the transit signal relative to each KOI host star via difference imaging. For each quarter, a difference image

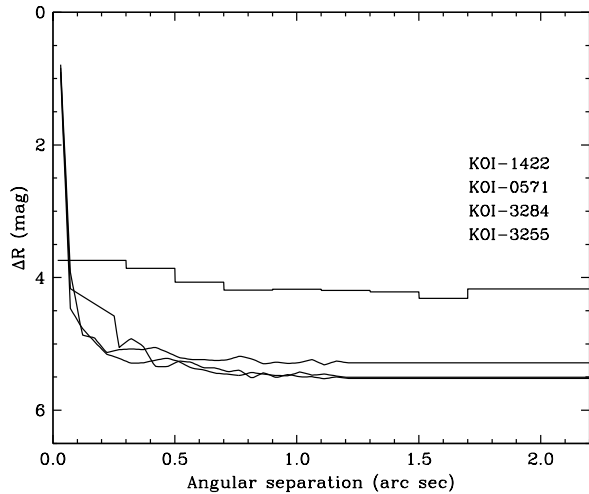


Figure 3. Similar to Figure 2 for the four targets observed with speckle interferometry at the Gemini North telescope. Curves are shown for the (692 nm) R -band observations, and correspond to the KOIs as labeled, top to bottom.

may be formed by subtracting an average of in-transit pixel values from out-of-transit pixel values. If the transit signal is due to a stellar source, the difference image will show that stellar source, whose location is determined by Pixel Response Function centroiding (PRF; see Bryson et al. 2010). This location may then be compared to the location of the host star, determined from a PRF-fit centroid of an average out-of-transit image (assuming the host is well isolated). Repeating this for each quarter in which transits occur gives a collection of offsets of the transit source from the host star. The average of these quarterly offsets defines the final offset of the transit source from the host star. This metric is reported for each KOI on the NASA Exoplanet Archive. If the offset is greater than three times its uncertainty, there is cause for concern that the signal may be coming from a background source rather than the KOI itself. In that case we would conclude that the likelihood that the transit signal is due to a planet around the KOI host star is low (for details, see Bryson et al. 2013). Any transit source location less than 3σ from the host star is considered statistically indistinguishable from the host star. This 3σ exclusion radius depends on the KOI rather than the host star, as it is primarily a function of the signal-to-noise ratio of the KOI’s transit signal.

Table 3 lists the average offset of the transit source for each KOI from the KOI host star, as reported on the Exoplanet Archive, as well as the 3σ exclusion radius for each KOI. All KOIs have offsets that are less than three times their uncertainties, with the exception of KOI-4427.01. Therefore, on centroid grounds alone KOI-4427.01 has a non-negligible chance of being a false positive.

The companions at $4''$ to $5''$ from KOI-2529, 3284, and 4427 listed in Table 2 are significantly farther than 3σ from the respective observed transit positions, so they are ruled out as possible sources of the transit, as are any wider companions detected in the UKIRT images. On the other hand, the close ($< 0''.5$) companions to KOI-1422, 2529, 3255, and 3284 cannot be ruled out by centroid analysis alone. We address this issue later. Additional closer (unresolved) companions may of course also be present.

Table 3
Centroid results for the candidates.

Candidate	Offset from star ($''$)	Offset from star (σ)	3σ exclusion radius ($''$)
KOI-0571.05	0.74 ± 0.82	0.90	2.45
KOI-1422.04	0.34 ± 0.34	1.00	1.03
KOI-1422.05	0.54 ± 0.33	1.67	0.98
KOI-2529.02	0.08 ± 0.64	0.13	1.92
KOI-3255.01	0.55 ± 0.19^a	2.82	0.58^a
KOI-3284.01	0.60 ± 0.94^a	0.64	2.82^a
KOI-4005.01	0.23 ± 0.61	0.38	1.84
KOI-4087.01	0.11 ± 0.41	0.26	1.22
KOI-4427.01	0.83 ± 0.24^b	3.47	0.72^b
KOI-4622.01	0.92 ± 0.52	1.76	1.57
KOI-4742.01	1.19 ± 1.17	1.01	3.52
KOI-4745.01	0.76 ± 0.36	2.09	1.08

^a The presence of relatively bright close companions to KOI-3255 and KOI-3284 can cause biases in the centroid measurements. These biases are expected to be smaller than the separation of the close companion, but we have nevertheless conservatively doubled the uncertainty found on the Exoplanet Archive.

^b The Exoplanet Archive reports the offset of KOI-4427.01 as $0''.94 \pm 1''.57$, but there is a single large outlier due to a quarter with a noisy difference image. The values reported here are after removing the outlier.

The centroid offsets in Table 3, on the basis of which we rule out the 4 – $5''$ companions, were computed on the assumption that the host stars do not have closer ($< 4''$) companions of comparable brightness. However, as described in Sect. 4.1, this is not the case for KOI-3255 and KOI-3284. The relatively bright close companions for these two KOIs will introduce error in the centroid measurement of the KOI star position. (Such error does not arise for the difference-image centroids measuring the transit source position because, assuming negligible variability, the difference image shows only the star hosting the transit signal.) To account for this unknown error, we have chosen to conservatively double the offset uncertainties for KOI-3255 and KOI-3284, although we do not expect the error to be larger than the separation of the companion. The uncertainties in the table already include this conservative doubling. The companion for KOI-2529 is sufficiently dim that the centroid error due to this companion should be negligible.

4.3. Optical spectroscopy

In order to characterize the target stars and search for additional companions, we acquired high-resolution spectra for the eleven stars in our sample with the Keck I Telescope on Mauna Kea (HI) and the HIRES spectrometer (Vogt et al. 1994), using the standard setup of the California Planet Search (CPS; see Howard et al. 2010). The wavelength coverage is approximately 3800 – 8000 \AA , recorded on three contiguous CCD detectors. Observations were made over the course of four nights (UT 2012 July 26 and September 22, and 2013 June 7 and 28) under clear skies, with a typical seeing of $\sim 1''$. Exposure times of about 15 minutes resulted in signal-to-noise ratios of 12 – 25 per pixel at a mean wavelength near the Mg I b triplet (5150 – 5200 \AA). The exception was KOI-3284, which was observed for 45 minutes yielding a SNR of 45 per pixel. All spectra were taken using the C2 decker ($0''.86 \times 14''$), giving a resolving power of $R \approx 60,000$. The $14''$ long slit allows for subtraction of

the sky background that is superimposed on the stellar spectrum. Sky subtraction was performed by measuring the sky background light on a wavelength-by-wavelength basis.

For the reduction of the raw spectra we used the standard CPS pipeline. Images from each of the three HIRES CCDs were independently reduced and subjected to sky subtraction, flat fielding, and cosmic ray removal. The pixel columns at each wavelength were then summed, providing photon counts as a function of wavelength for each pixel. Consistent wavelength solutions were ensured by aligning a carefully chosen set of Thorium-Argon emission lines onto the same pixels at the beginning of each night’s observations.

The radial velocity (RV) of each star was measured using the A-band and B-band telluric line features as wavelength fiducials. We measured the placement of the stellar absorption lines relative to these features, and then referenced them to stars of known radial velocity (Chubak et al. 2012). The final radial velocity measurements in the frame of the solar system barycenter are accurate to $\pm 0.1 \text{ km s}^{-1}$, and are given in Table 4 with other details of the observations.

To aid in eliminating some of the false positives that might be causing the transit-like signals in our targets, we searched each of our spectra for evidence of a second set of lines from another star possibly falling on the spectrometer slit during our observations (i.e., at angular separations smaller than about $0''.43$, or half of the slit width). We first cross-correlated each spectrum against a large library of stellar spectra obtained with the same instrument and setup (see Sect. 5) in order to identify the best match. After flux normalization and placement of the target star and library stars onto a common wavelength solution, we subtracted this best match from the observed spectra, and the residuals were subsequently cross-correlated against the same set of library stars (Kolbl et al. 2015). A resulting peak in the cross-correlation function would be evidence of a second star contaminating the spectrum. For our targets this method is sensitive to physically associated as well as unrelated (background/foreground) companion stars so long as the relative RV of the two objects is greater than about 10 km s^{-1} . For smaller velocity differences the technique loses sensitivity due to imperfect subtraction of the primary star.

We detected no companions to any of the 11 stars in our sample down to about 1% of the brightness of the primary (corresponding to a magnitude difference $\Delta Kp = 5$) for targets brighter than $Kp = 15$, and down to 2% ($\Delta Kp \approx 4.2$) for our fainter targets. This indicates that at least two of the close companions found in our Keck AO imaging that are bright enough to have been detected spectroscopically, those around KOI-3255 and KOI-3284, must have radial velocities within 10 km s^{-1} of the main star, which strongly suggests they are physically associated with the target.

4.4. Near-infrared spectroscopy

For two of our cooler targets (KOI-4087 and KOI-4622) we gathered near-infrared spectra with the TripleSpec instrument (Herter et al. 2008) on the Apache Point Observatory 2.5 m telescope to supplement the material described above and to aid in the determination of the stel-

Table 4
Spectroscopic observations (Keck/HIRES).

Star	BJD (2,400,000+)	Exposure (sec)	SNR (pix ⁻¹)	RV (km s ⁻¹)
KOI-0571	56135.11242	900	18	-61.7
KOI-1422	56192.77304	900	13	-24.8
KOI-2529	56472.07615	900	13	-12.2
KOI-3255	56472.06602	729	24	-15.3
KOI-3284	56450.88292	2700	45	-90.9
KOI-4005	56472.05630	785	25	-41.0
KOI-4087	56472.04532	900	15	-20.1
KOI-4427	56472.03348	900	12	-11.6
KOI-4622	56472.08746	900	15	-98.6
KOI-4742	56472.02224	900	20	-76.2
KOI-4745	56472.09849	900	14	-24.0

lar properties (Sect. 5). For both observations, taken on UT 2014 June 26, we used the $1''.1$ slit giving a resolving power of $R \approx 3500$. We alternated exposures in an ‘ABBA’ fashion, integrating for 4 minutes at each position until we achieved a SNR of at least 80 per pixel throughout the *H* band (our SNR is slightly higher, about 100, for KOI-4622). Our total integrations were 48 minutes and 64 minutes for KOI-4087 and KOI-4622, respectively. We took care to gather spectra of the A0 V telluric standard star 51 Dra (using an exposure time of 10s per image in the same ABBA nod strategy) at intervals separated by no more than 30 minutes in time from the KOI observations, corresponding to changes in airmass of 0.1 from the positions of the KOIs. We also gathered flat field images using the bright quartz lamp at the Apache Point Observatory. We used the `spectool` pipeline (Cushing et al. 2004) to co-add flat fields and science frames and to extract the spectra from the full-frame images. The `xtellcor` package was then employed to compare the spectra of our standard A0 V star 51 Dra to that of Vega, in order to identify and remove telluric absorption lines in both KOI spectra.

5. STELLAR PROPERTIES

We used our Keck/HIRES spectra to estimate the effective temperature (T_{eff}), surface gravity ($\log g$), and metallicity ($[\text{Fe}/\text{H}]$) of our stars using a procedure referred to as `SpecMatch` (Petigura et al., in prep.). `SpecMatch` compares an observed target spectrum against a set of approximately 800 library spectra obtained with the same instrument that span a wide range of parameters ($T_{\text{eff}} = 3500\text{--}7500 \text{ K}$, $\log g = 2.0\text{--}5.0$ (cgs), and $[\text{Fe}/\text{H}]$ values from -1.0 to $+0.5$ dex). For each comparison `SpecMatch` places the target spectrum onto the same wavelength scale as the library spectrum and computes χ^2 , the sum of the squares of the pixel-by-pixel differences in normalized intensity. We adopted the mean T_{eff} , $\log g$, and $[\text{Fe}/\text{H}]$ of the ten closest matching library spectra (weighted by the χ^2) as the final set of stellar parameters for each target spectrum. They are reported in Table 5 for about half of our sample. We estimate these parameters to be accurate to about 100 K in T_{eff} , 0.10 dex in $\log g$, and 0.10 dex in $[\text{Fe}/\text{H}]$ based on comparisons with benchmark stars having parameters measured using detailed LTE modeling.

For stars cooler than about 4300 K this technique becomes less reliable. In that temperature range the library of reference spectra is quite sparse, and it is possible for

Table 5
Spectroscopic parameters.

Star	T_{eff} (K)	$\log g$ (cm s^{-2})	[Fe/H] (dex)	Source
KOI-0571	3755 ± 90	...	-0.26 ± 0.12	1,2
KOI-1422	3572 ± 80	...	-0.12 ± 0.12	1,2
KOI-2529	4651 ± 100	4.64 ± 0.10	$+0.01 \pm 0.10$	3
KOI-3255	4551 ± 100	4.67 ± 0.10	0.00 ± 0.10	3
KOI-3284	3748 ± 112	...	$+0.16 \pm 0.14$	2
KOI-4005	5431 ± 100	4.50 ± 0.10	$+0.02 \pm 0.10$	3
KOI-4087	4134 ± 154	...	-0.30 ± 0.15	4
KOI-4427	3813 ± 112	...	-0.07 ± 0.14	2
KOI-4622	4340 ± 177	...	-0.57 ± 0.18	4
KOI-4742	4402 ± 100	4.71 ± 0.10	-0.37 ± 0.10	3
KOI-4745	4723 ± 100	4.62 ± 0.10	-0.01 ± 0.10	3

Note. — Sources are: 1. Mann et al. (2013a,b); 2. Muirhead et al. (2014); 3. **SpecMatch**; 4. New estimates from this paper.

the **SpecMatch** T_{eff} value to be biased high simply because the best matches are hotter. Similar biases are likely in $\log g$ and [Fe/H].¹⁹ Six stars in our sample are in this regime: KOI-0571, 1422, 3284, 4087, 4427, and 4622. Spectroscopic parameters (except for $\log g$) for the first three and for KOI-4427 were reported by Mann et al. (2013a,b) and/or Muirhead et al. (2014)²⁰ based on the measurement of temperature- and metallicity-sensitive features in near infrared H -band or K -band spectra. We adopted averages of those determinations here.

For KOI-4087 and KOI-4622 we derived new parameters based on the NIR spectra described in Sect. 4.4. Effective temperatures were inferred from the empirical H -band calibrations of Newton et al. (2015), which were established using stars with bolometric luminosities and temperatures from long-baseline interferometry (Boyajian et al. 2013). They are valid between 3100 K and 4800 K, and have a typical scatter of 72 K. Spectral indices based on the Mg I doublet at $1.50 \mu\text{m}$ and the Al I doublet at $1.67 \mu\text{m}$ were measured as described by Newton et al. (2015), and temperature uncertainties were obtained from numerical simulations following the same work. Metallicities for KOI-4087 and KOI-4622 were determined using the NIR calibrations of Mann et al. (2013c), which have the advantage over other calibrations developed in recent years (Rojas-Ayala et al. 2010, 2012; Terrien et al. 2012; Newton et al. 2014a) that they were established including K dwarfs with effective temperatures greater than 4000 K. They are thus the most appropriate calibrations for these two KOIs, which lie on the K/M-dwarf boundary. Mann et al. (2013c) showed that the K -band relations display the strongest correlation with [Fe/H]. We adopted their calibration in Eq.(16), which has a scatter of 0.11 dex. The analysis of the spectra, the measurement of the spectral features (equivalent widths of the $2.21 \mu\text{m}$ Na I doublet, the CO (2-0) band-head in the K band, and the $\text{H}_2\text{O-K2}$ index from Rojas-Ayala et al. 2012), as well as the uncertainty estimation followed the

¹⁹ Even though **SpecMatch** has difficulty obtaining accurate parameters for cool stars, it is still easily capable of distinguishing dwarfs from giants as the pressure-sensitive lines such as the Mg I b triplet are very much narrower in giants than in our dwarf library spectra. All of the targets in this paper are verified to be dwarfs.

²⁰ The Muirhead et al. (2014) values supersede earlier ones reported by Muirhead et al. (2012) that used the same spectra.

procedures described recently by Muirhead et al. (2014), who applied the same methodology to a similar set of spectra of about 100 M-dwarf KOIs. The new temperatures and metallicities for KOI-4087 and KOI-4622 may be found in Table 5.

The spectroscopic parameters for our targets were used to estimate the stellar properties (primarily the mass and radius) by appealing to stellar evolution models from the Dartmouth series (Dotter et al. 2008), following a Monte Carlo procedure similar to that described by Torres et al. (2008). While this is straightforward for the stars with complete information (T_{eff} , [Fe/H], and $\log g$), we lack a $\log g$ estimate for the six cooler stars because the spectroscopic techniques applied to them do not constrain that property. Thus, we cannot establish their precise ages, or equivalently, their sizes. This uncertainty is relatively unimportant, however, because the radii of cool main-sequence stars change little with age. Most of those stars show periodic brightness variations that may be interpreted as rotational modulation, and in principle knowledge of the rotation periods (P_{rot}) enables one to infer a rough age using gyrochronology relations. The age, in turn, may be used in place of $\log g$ as a constraint for the stellar evolution modeling, although in practice the constraint is weak because the radius is not very sensitive to age, as just stated. Our determination of P_{rot} for KOI-3284, 4087, 4427, and 4622 is explained in the following section; for KOI-0571 and KOI-1422 we adopted the periods measured previously by others (see below). Our age estimates relied on the gyrochronology relations of Epstein & Pinsonneault (2014), which are claimed to provide values good to ~ 1 Gyr for stars with masses above $0.55 M_{\odot}$, degrading rapidly below that. The $B-V$ color indices required by these calibrations were taken from the UBV survey of the *Kepler* field by Everett et al. (2012), along with reddening values from the KIC. Generous uncertainties of 0.1 mag were assigned to the dereddened color indices to account for possible systematic errors. For KOI-1422 and KOI-3284 the colors were additionally corrected for the presence of the close companions described in Sect. 4.1, assuming they are physically associated. The formal ages inferred for KOI-0571, 1422, 3284, 4087, and 4622 are $3.89^{+0.62}_{-0.51}$, $3.57^{+3.25}_{-3.21}$, $4.36^{+0.76}_{-0.61}$, $1.20^{+0.39}_{-0.52}$, and $1.82^{+0.44}_{-0.31}$ Gyr, respectively. As described below, KOI-4427 does not display a clear signature of rotation, so we have conservatively adopted a broad interval of possible rotation periods (10–45 days) based on the full range of periods observed for M stars of similar temperature, as reported by McQuillan et al. (2013) (see their Fig. 10). The corresponding age range from the gyrochronology relations of Epstein & Pinsonneault (2014) is 1–6 Gyr, which we then used as a constraint for the isochrone modeling.

KOI-0571 and KOI-1422 are systems with multiple transiting planet candidates (five each). In such cases, if the candidates can be assumed to transit the same star in near-circular orbits (required for stability), the transit light curve modeling can provide a much stronger constraint on the mean stellar density (ρ_{\star}) than for single-planet candidates because the density estimates from the different candidates within the same system can be averaged together (see Sect. 8.1). For these two KOIs we have therefore made use of the photometric ρ_{\star} in our Monte

Carlo procedure simultaneously with the age constraint to strengthen the determination of the stellar characteristics.

The final properties from our stellar evolution modeling are listed in Table 6, computed from the mode of the corresponding posterior distributions. Uncertainties correspond to the 68.3% (1σ) credible intervals from the same distributions. Distances were computed from the absolute K_s magnitudes inferred from the isochrones along with the apparent brightness from the Two Micron All-Sky Survey (2MASS; Cutri et al. 2003) in the same passband, which is the one least affected by interstellar extinction. We nevertheless made corrections for extinction that we inferred from reddening values for each KOI adopted from the KIC, as above. For the four targets with close companions (KOI-1422, 2529, 3255, and 3284) the apparent magnitudes were corrected for the light contribution of the neighbors. On the assumption that those stars are physically bound to the targets, their typical orbital semimajor axes would be approximately 52, 248, 75, and 64 AU, and their orbital periods roughly 550, 4600, 770, and 690 yr, respectively.

5.1. Stellar rotational periods

Here we give the details of our determination of the rotation periods used above for four of the cooler targets in our sample that have no spectroscopic estimate of $\log g$: KOI-3284, 4087, 4427, and 4622. For this application the processing of the raw photometry was somewhat different than that described earlier, because we wished to retain the astrophysical variations present in the light curve while at the same time removing the instrumental effects. We therefore used the Presearch Data Conditioning Maximum A-Posteriori (PDC-MAP) data from *Kepler* (Smith et al. 2012), which is designed to meet those goals.

Since the data are unevenly sampled and each quarter has a unique offset, we elected to use a Lomb-Scargle style periodogram.²¹ The light curve model is a simple sinusoid and thus is linear with respect to the model parameters for any trial rotation period, P_{rot} . Using weighted linear least squares we are guaranteed to find the global maximum likelihood solution at each trial P_{rot} . We scanned in frequency space from twice the cadence up to twice the total baseline of observations, taking 10^5 uniform steps in frequency. At each realization, we defined the “power” as $(BIC_{\text{null}} - BIC_{\text{trial}})/BIC_{\text{null}}$, where BIC is the Bayesian Information Criterion and “null” and “trial” refer to the two models under comparison. We also performed a second periodogram analysis with a finer grid step around any prominent peaks found in the original periodograms.

The resulting periodograms for KOI-3284, 4087, 4427 and 4622 are shown in Figure 4. KOI-3284 and KOI-4087 show clear uni-modal peaks at 37.53 ± 0.73 d and

²¹ Stars with active regions have a non-uniform surface brightness distribution, leading to brightness variations as the star rotates (Budding 1977). These active regions tend to evolve in location and amplitude over timescales of days to years, which can cause the periodicities to change as well due to differential rotation (Reinhold et al. 2013). Despite the complex nature of individual spots, the ensemble population tends to imprint the rotation period as a dominant peak in the Fourier domain, allowing for an estimate of the rotation period using photometry alone (Basri et al. 2011; Nielsen & Karoff 2012).

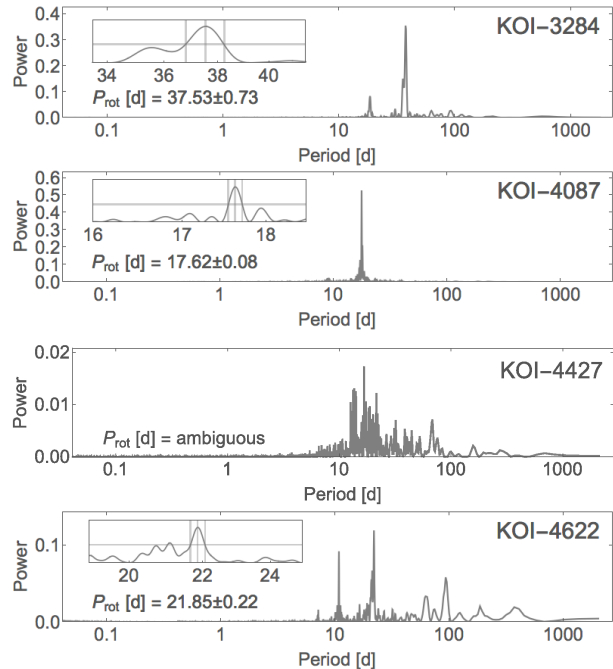


Figure 4. Periodograms of the *Kepler* PDC-MAP photometry for four of the KOIs for which a spectroscopic surface gravity constraint is lacking. The insets show a close-up of the main peak, with an indication of the full width at half maximum that we assign as the error in P_{rot} . No clear result is obtained for KOI-4427.

17.62 ± 0.08 d, respectively, which we attribute to their rotation periods. Here we have taken the 1σ confidence intervals to be the full width of the peak in the periodogram at half maximum. For comparison, we note that McQuillan et al. (2013) used an autocorrelation periodogram and found peaks at similar periods (37.026 d and 17.542 d). Additionally, KOI-4087 is in the sample studied by Nielsen et al. (2013), who obtained $P_{\text{rot}} = 17.496$ d, in good agreement with the other results. KOI-4427 shows no clear peaks above the noise level, in agreement with the findings of McQuillan et al. (2013), so we were unable to assign a rotation period in this case. A possible reason for complex structure of the periodogram in this case is the presence of other unresolved stars in the aperture.

KOI-4622 exhibits two peaks and is not included in either the McQuillan et al. (2013) or the Nielsen et al. (2013) samples. The dominant peak occurs at 21.85 ± 0.22 d, with a second peak at $\sim 25\%$ lower power with $P = 10.72 \pm 0.06$ d. We note that this second peak occurs not only at a lower power but also at nearly exactly one half the period of the higher peak. We argue that the longer period is that of the stellar rotation, and the shorter period is an alias caused by more than one active region on the stellar surface.

Two other cool KOIs have had their rotation periods determined previously (33.70 ± 0.31 d for KOI-0571 and 36.5 ± 17.6 d for KOI-1422; McQuillan et al. 2013), and we adopt those values here as published.

6. CANDIDATE VALIDATION

The Doppler signals (velocity semi-amplitudes) expected of the candidates in our sample, if due to planets around the targets, range from 0.4 to 1.4 m s^{-1} based on rough estimates of their masses using the prelim-

Table 6
Stellar properties.

Star	Age (Gyr)	M_\star (M_\odot)	R_\star (R_\odot)	$\log g$ (cm s^{-2})	ρ_\star (g cm^{-3})	L_\star (L_\odot)	M_V (mag)	M_{K_s} (mag)	Distance (pc)
KOI-0571	$4.0^{+0.6}_{-0.6}$	$0.544^{+0.024}_{-0.021}$	$0.523^{+0.023}_{-0.021}$	$4.736^{+0.020}_{-0.019}$	$5.29^{+0.54}_{-0.39}$	$0.055^{+0.011}_{-0.006}$	$9.01^{+0.24}_{-0.24}$	$5.41^{+0.14}_{-0.15}$	172^{+13}_{-10}
KOI-1422	$4.2^{+3.4}_{-1.6}$	$0.454^{+0.033}_{-0.035}$	$0.426^{+0.038}_{-0.027}$	$4.833^{+0.025}_{-0.041}$	$7.94^{+1.34}_{-1.08}$	$0.027^{+0.008}_{-0.004}$	$10.12^{+0.25}_{-0.35}$	$6.07^{+0.20}_{-0.23}$	226^{+28}_{-18}
KOI-2529	$3.0^{+7.7}_{-0.3}$	$0.729^{+0.033}_{-0.029}$	$0.697^{+0.028}_{-0.023}$	$4.619^{+0.015}_{-0.028}$	$3.03^{+0.24}_{-0.25}$	$0.199^{+0.039}_{-0.025}$	$6.98^{+0.25}_{-0.24}$	$4.36^{+0.11}_{-0.11}$	618^{+34}_{-30}
KOI-3255	$2.9^{+7.5}_{-0.3}$	$0.707^{+0.033}_{-0.027}$	$0.680^{+0.026}_{-0.024}$	$4.629^{+0.015}_{-0.026}$	$3.18^{+0.25}_{-0.25}$	$0.173^{+0.035}_{-0.022}$	$7.20^{+0.26}_{-0.24}$	$4.45^{+0.11}_{-0.11}$	417^{+24}_{-21}
KOI-3284	$4.4^{+0.8}_{-0.7}$	$0.544^{+0.041}_{-0.061}$	$0.520^{+0.038}_{-0.061}$	$4.740^{+0.059}_{-0.029}$	$5.52^{+1.53}_{-0.77}$	$0.044^{+0.017}_{-0.012}$	$9.55^{+0.54}_{-0.44}$	$5.50^{+0.41}_{-0.25}$	145^{+20}_{-23}
KOI-4005	$7.2^{+3.6}_{-0.2}$	$0.884^{+0.044}_{-0.038}$	$0.866^{+0.076}_{-0.040}$	$4.514^{+0.035}_{-0.073}$	$1.89^{+0.30}_{-0.38}$	$0.581^{+0.153}_{-0.079}$	$5.46^{+0.21}_{-0.25}$	$3.69^{+0.12}_{-0.19}$	693^{+66}_{-38}
KOI-4087	$1.3^{+0.6}_{-0.2}$	$0.575^{+0.043}_{-0.047}$	$0.559^{+0.029}_{-0.054}$	$4.706^{+0.049}_{-0.016}$	$4.76^{+1.03}_{-0.48}$	$0.079^{+0.023}_{-0.022}$	$8.33^{+0.55}_{-0.32}$	$5.02^{+0.42}_{-0.13}$	261^{+16}_{-46}
KOI-4427	$3.6^{+2.6}_{-1.3}$	$0.526^{+0.040}_{-0.062}$	$0.505^{+0.038}_{-0.065}$	$4.751^{+0.067}_{-0.030}$	$5.79^{+1.87}_{-0.82}$	$0.043^{+0.017}_{-0.012}$	$9.34^{+0.57}_{-0.41}$	$5.54^{+0.42}_{-0.24}$	240^{+32}_{-39}
KOI-4622	$1.9^{+0.5}_{-0.4}$	$0.572^{+0.049}_{-0.053}$	$0.550^{+0.038}_{-0.054}$	$4.715^{+0.047}_{-0.024}$	$4.94^{+1.03}_{-0.66}$	$0.089^{+0.038}_{-0.026}$	$8.02^{+0.62}_{-0.44}$	$5.00^{+0.41}_{-0.20}$	284^{+28}_{-48}
KOI-4742	$2.9^{+8.1}_{-0.2}$	$0.609^{+0.030}_{-0.026}$	$0.598^{+0.023}_{-0.024}$	$4.673^{+0.018}_{-0.021}$	$4.01^{+0.37}_{-0.30}$	$0.117^{+0.024}_{-0.016}$	$7.73^{+0.28}_{-0.25}$	$4.79^{+0.15}_{-0.11}$	342^{+19}_{-22}
KOI-4745	$3.2^{+7.5}_{-0.4}$	$0.738^{+0.033}_{-0.029}$	$0.706^{+0.028}_{-0.024}$	$4.614^{+0.016}_{-0.029}$	$2.96^{+0.24}_{-0.25}$	$0.217^{+0.043}_{-0.027}$	$6.83^{+0.25}_{-0.23}$	$4.32^{+0.11}_{-0.11}$	779^{+45}_{-38}

Note. — Ages, $\log g$, and ρ_\star are best-fit values from the Dartmouth models, constrained by either a spectroscopic $\log g$, a light-curve-derived ρ_\star , and/or a gyrochronology age based on the rotation period (see text).

inary radius measures and the mass-radius relation of Weiss & Marcy (2014). Given the faintness of the parent stars ($Kp = 14.3\text{--}15.9$), the detection of such small variations would be very challenging, and therefore the planetary nature of these objects cannot presently be “confirmed” in the usual way, i.e., by establishing that the orbiting objects are of planetary mass. Instead they must be “validated” statistically, by showing that the likelihood of a true planet (which we refer to hereafter as the ‘planet prior’) is orders of magnitude larger than that of a false positive. We describe this process below.

6.1. Overview

The types of astrophysical false positives we consider in our analysis involve other unseen stars in the photometric aperture of *Kepler* that are eclipsed by an orbiting object, and have their eclipses attenuated by the light of the target such that they mimic shallow planetary transits. Examples of these situations include background or foreground eclipsing binaries (‘BEB’), background or foreground stars transited by a (larger) planet (‘BP’), and physically associated stars transited by a smaller star or by a planet. Such physically associated stars will typically be close enough to the target that they are generally unresolved in high-resolution imaging. We refer to these hierarchical triple configurations as ‘HTS’ or ‘HTP’, depending on whether the object orbiting the physical companion is a star or a planet.²²

The procedure we used for validation is BLENDER (Torres et al. 2004, 2011; Fressin et al. 2012), which

²² We point out that other statistical studies using *Kepler* data (e.g., Morton & Johnson 2011; Morton 2012; Lissauer et al. 2014) have not considered the HTP scenario as a false positive, arguing that the exact location of the planet (whether on the intended target or a bound companion) is inconsequential although its size may be larger if around the companion. Validation without considering these kinds of false positives is significantly easier, particularly since they tend to dominate the blend frequency, as we show below. For the present work, however, planet size is critical because it affects habitability: a planet that transits an unseen companion instead of the target may be too large to be rocky, and is thus less interesting for our purposes (see, e.g., Alibert 2014; Rogers 2014). We therefore count HTP configurations as blends.

has been applied successfully in the past to many of the most interesting candidates revealed by *Kepler* (see, e.g., Borucki et al. 2013; Barclay et al. 2013; Meibom et al. 2013; Ballard et al. 2013; Kipping et al. 2014b). BLENDER makes full use of the detailed shape of the transits to limit the pool of viable blends. It does this by simulating large numbers of blend scenarios and comparing each of them with the *Kepler* photometry in a χ^2 sense. Fits that give the wrong shape for the transit are considered to be ruled out. This enables us to place useful constraints on the properties of the objects that make up the blend, including their sizes and masses, overall color and brightness, the linear distance between the background/foreground eclipsing pair and the target, and even the eccentricities of the orbits. Those constraints are then used to estimate the frequencies of blends of different kinds. We note that the simulated light curves generated by BLENDER take full account of any known extra light in the aperture, such as that coming from the close companions reported earlier (see Table 2). We also point out that here we only consider blends involving main-sequence stars, as BEBs with a giant component produce light curves with a shape that does not mimic a true planetary transit when observed with such high precision as delivered by *Kepler*.

The photometric data we use here are the long-cadence PDC-MAP time series, as in Sect. 5.1, detrended to remove signals at time scales long compared to the transit durations. Throughout this analysis we followed the nomenclature established in previous BLENDER studies, designating the objects in the eclipsing pair as the “secondary” and “tertiary”, and the target itself as the “primary”. We drew stellar properties for the primary, secondary, and tertiary (masses, radii, and absolute brightness in the *Kepler* and other passbands) from model isochrones from the Dartmouth series (Dotter et al. 2008); the selection of the isochrone for the primary was based on the spectroscopic properties given earlier. The BLENDER studies cited above may be consulted for further technical details.

In summary, our validations proceed in two stages.

First, we use BLENDER proper to derive constraints on blend scenarios from their light curve shapes. Then, we incorporate other constraints from follow-up observations to compute the blend frequencies and the planet prior by means of Monte Carlo simulations. We now address each of these steps in turn.

6.2. BLENDER constraints

To illustrate the constraints derived from the shape of the transit, we focus here on one of our candidates, KOI-4005.01. BLENDER indicates that background eclipsing binaries are only able to produce viable false positives if the primary star of the eclipsing pair is restricted to a narrow range of main-sequence masses²³ between about $0.7 M_{\odot}$ and $1.4 M_{\odot}$, and to a limited interval in brightness (Kp magnitude) relative to the target corresponding to $\Delta Kp \leq 5.5$. Figure 5 shows the χ^2 landscape for all blends of this kind (BEB scenario) in a representative cross-section of parameter space. Regions outside of the 3σ contour correspond to configurations with light curves giving a poor fit to the observations, i.e., much worse than a true planet fit. These blends are therefore excluded. The figure also illustrates some of the additional constraints available from our follow-up observations for this candidate. For example, analysis of our Keck/HIRES spectra of KOI-4005 generally rules out companions within 5 magnitudes of the primary if they are angularly close enough to fall within the spectrograph slit.²⁴ This can eliminate much of parameter space (see green hatched area in the figure²⁵). Additionally, by comparing the $r - K_s$ colors of the simulated blends with the measured color index of the target ($r - K_s = 1.580 \pm 0.029$; Brown et al. 2011), we find that some of the BEB scenarios we have simulated are either too blue or too red by more than 3σ (blue hatched areas in the figure), and are therefore also excluded. However, for this particular KOI all BEB blends with the wrong color are already excluded by BLENDER for giving poor fits (i.e., they are outside of the 3σ contour). Santerne et al. (2013) have pointed out that an additional source of blends involves eclipsing binaries with eccentric orbits that are oriented so that they show only a secondary eclipse, as viewed by *Kepler*. More generally, we note that they could also show only a primary eclipse. We find, though, that while the depth and shape of the diluted eclipses may indeed match the transit signal in some cases, the combined color and brightness of these blends are such that they are generally ruled out by the spectroscopic constraint and/or the measured color of the KOI.

²³ Stars more massive than about $1.4 M_{\odot}$ will generally have evolved to become giants for ages typical of the field (~ 3 Gyr), and such stars yield light curves that have a very different shape than a transit, as stated earlier, so they do not constitute viable blends.

²⁴ For typical seeing conditions at the Keck telescope stars that are beyond $0''.43$ can still imprint their lines on the target spectrum, and be detected, as can stars at wider separations that happen to be aligned along the slit. Nevertheless, to be conservative we assume here that these companions are spectroscopically undetectable.

²⁵ Note, however, that not all blends in the green hatched area are excluded. This is only the case if the background star falls on the slit, and its RV is more than 10 km s^{-1} different from that of the target. In all other cases we consider the blends to be viable, even if they have $\Delta Kp < 5$.

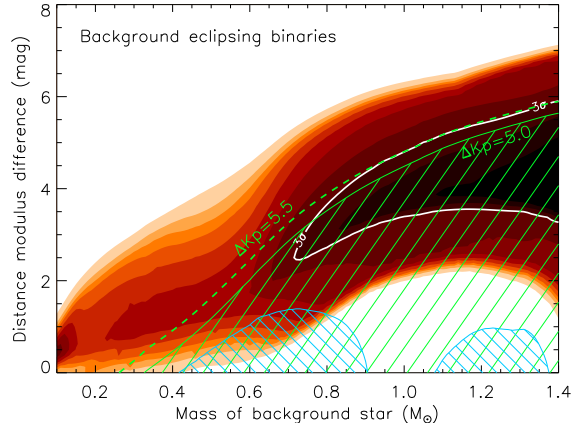


Figure 5. Map of the χ^2 surface (goodness of fit) for KOI-4005.01 corresponding to blends involving background eclipsing binaries. On the vertical axis we represent the linear distance between the BEB and the target ($D_{\text{BEB}} - D_{\text{target}}$), expressed for convenience in terms of the difference in distance modulus, $\Delta\delta = 5 \log(D_{\text{BEB}}/D_{\text{target}})$. Only blends within the solid white contour (darker colors) provide fits to the *Kepler* light curve that are within acceptable limits (3σ , where σ is the significance level of the χ^2 difference compared to a transiting planet model fit; see Fressin et al. 2012). Other concentric colored areas (lighter colors) represent fits that are increasingly worse (4σ , 5σ , etc.), which we consider to be ruled out. The blue cross-hatched areas correspond to regions of parameter space where the blends are either too red (left) or too blue (right) compared to the measured $r - K_s$ color of the target, by more than three times the measurement uncertainty. The dashed green line labeled $\Delta Kp = 5.5$ is tangent to the white contour from above and corresponds to the faintest viable blends. The green line labeled $\Delta Kp = 5.0$ represents the spectroscopic limit on faint background stars. All simulated blends below this line (green hatched region) are brighter and are generally excluded if the BEB is angularly close enough to the target to fall within the slit of the spectrograph. Thus, very few blends remain viable.

For blends involving a background or foreground star transited by a planet (BP scenario) there is a wide range of secondary masses that produce good fits to the *Kepler* photometry of KOI-4005, as shown in Figure 6. BLENDER indicates that the faintest of these blends are about 5.8 magnitudes fainter than the target in the Kp passband. In this case, however, the spectroscopic and color constraints drastically reduce the pool of viable false positives.

The χ^2 map for blends involving a physically associated companion to KOI-4005 transited by a larger planet (HTP scenario) is seen in Figure 7, and shows the size of the tertiary as a function of the mass of the companion star (secondary). In this case BLENDER restricts the false positives to be in a narrow strip of parameter space corresponding to secondary masses larger than about $0.25 M_{\odot}$, and planetary sizes between 0.25 and about $0.8 R_{\text{Jup}}$ ($2.8\text{--}9.0 R_{\oplus}$). As in the other scenarios, color and brightness constraints allow us to reject many of these blends.

Finally, BLENDER indicates that pairs of eclipsing stars orbiting the target (HTS scenario) invariably produce light curves with the wrong shape for a transit, or feature noticeable secondary eclipses that are not observed in the photometry of KOI-4005.01, or, if they show only a single eclipse due to a high eccentricity and special orientation (Santerne et al. 2013), the overall brightness would make the eclipsing binary detectable and/or its

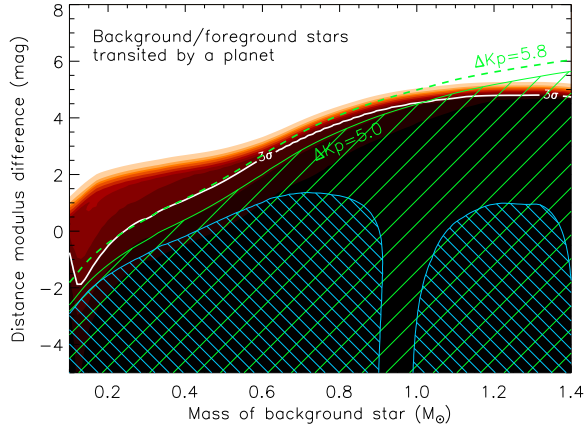


Figure 6. Similar to Figure 5 (and with the same color scheme) for blends involving background or foreground stars transited by a planet (BP scenario). The faintest blends giving acceptable fits have $\Delta Kp = 5.8$ relative to the target (dashed green line). Blends below the solid green ($\Delta Kp = 5.0$, hatched green area) are generally excluded by the spectroscopic constraint unless the intruding star is more than $0''.43$ from the target, or closer than $0''.43$ but with $\Delta RV < 10 \text{ km s}^{-1}$ (see text).

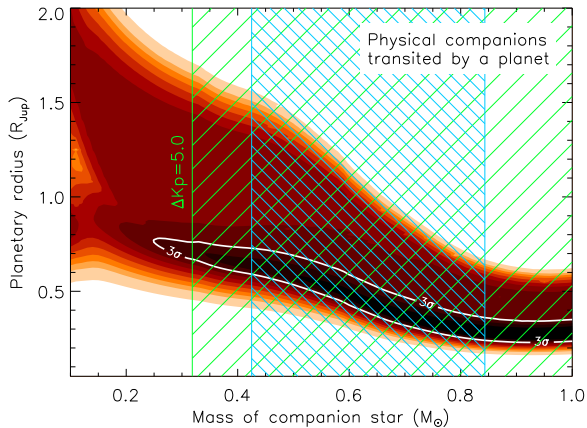


Figure 7. Similar to Figure 5 for the case of physical companions to KOI-4005 that are transited by a planet (HTP). Only companion stars with masses larger than about $0.85 M_{\odot}$ or smaller than about $0.42 M_{\odot}$ yield blend colors that are consistent with the measured $r - K_s$ index of KOI-4005. However, many of these blends are eliminated by the spectroscopic constraint, as they are brighter than $\Delta Kp = 5.0$.

color inconsistent with the measurement. These types of configurations are therefore easily excluded. A similar result was found for each of the other candidates in our sample, and indeed all previous BLENDER analyses of KOIs have also found that HTS blends are always ruled out with photometry of the quality delivered by the *Kepler* instrument, when combined with the observational constraints. Consequently, we do not consider HTS scenarios any further.

Maps of the χ^2 landscapes for the BEB, BP, and HTP scenarios analogous to those described above, along with the additional restrictions based on the color and the spectroscopic brightness limits, are shown for each of our other candidates in Figure set 8–10.

6.3. Estimating blend frequencies and the planet prior

The BLENDER constraints just described significantly reduce the number of viable BEB, BP, and HTP blends, but not all of the ones that remain can be ruled out by our follow-up observations. The next step of the analysis is therefore to quantify their expected frequencies, which we did via Monte Carlo simulations. Specifically, we generated large numbers of realistic false positives according to each of the blend scenarios, we eliminated those that BLENDER tells us would not match the *Kepler* light curve or that would have been detected in our follow-up observations, and we counted the survivors. These numerical experiments rely on the known distributions of binary star properties, the number density of stars near each target, and estimates of the rates of occurrence of transiting planets and of eclipsing binaries from the *Kepler* Mission itself. Those rates of occurrence (as well as any dependence they may have on orbital period or other properties) are implicit in the lists of KOIs and eclipsing binaries generated by the *Kepler* team (Burke et al. 2014; Slawson et al. 2011) that we used in our analysis, when normalized by the total number of targets observed by the spacecraft. Since we have recently made significant enhancements in these Monte Carlo procedures compared to previous applications, we take the opportunity to describe them in some detail here.

For the HTP scenario we simulated companion stars to each target following the distributions of binary properties (mass ratios, orbital periods, eccentricities) proposed by Raghavan et al. (2010) and Tokovinin (2014). We placed the companions in random orbits around the target assuming isotropically distributed inclination angles (i) and uniformly distributed longitudes of periastron (ω), as well as random orbital phases. Other relevant properties of these simulated companions (size, absolute magnitudes, and colors corresponding to their simulated masses) were inferred from the same isochrone used for the target, as the two stars are assumed to be coeval in this scenario. In particular, we computed the distance to the system by imposing the condition that the total apparent brightness of the two stars (accounting for extinction) must be the same as the Kp magnitude associated with the KOI, and this in turn enables us to compute the angular separation. We then assigned to each of these secondary stars a random transiting planet drawn from the actual list of KOIs hosted at the NASA Exoplanet Archive (list downloaded on 2014 March 26), which ensures that their properties (including any correlations among them) are as realistic as possible.²⁶ We accepted only planets with periods similar to the KOI under investigation (within a factor of two). The rationale for this is that the relevant HTP blend frequency is that of configurations that involve planets with periods near that of the candidate, as those frequencies depend strongly on orbital period. We then examined the properties of the stellar companions and their planets, and rejected scenarios that do not satisfy the BLENDER restrictions on companion mass, planetary size, and orbital eccentricity of the planet (related to the transit

²⁶ As pointed out by Lissauer et al. (2014), when attempting to validate targets with a single transiting planet candidate it is more appropriate to exclude from the list of known KOIs all stars with multiple candidates, as this unduly inflates the rates of occurrence of planets (particularly small ones that are more common in multiple systems). We have followed this recommendation here.

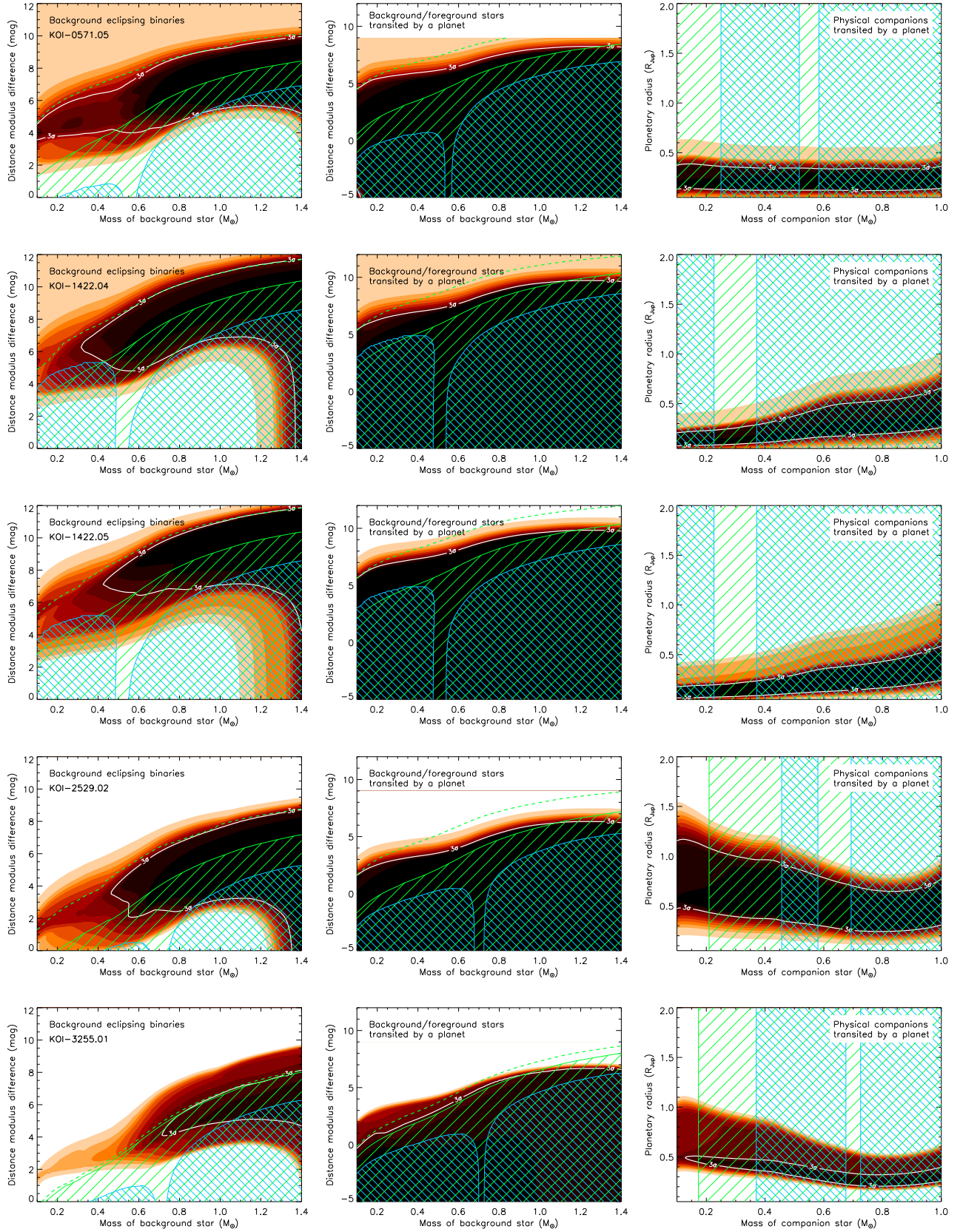


Figure 8. BLENDER χ^2 landscapes for five KOI targets. Each row corresponds to the KOI labeled in the left panel, and shows the three blend scenarios. Observational constraints from spectroscopy and color are also shown. See Figures 5–7 for a detailed description.

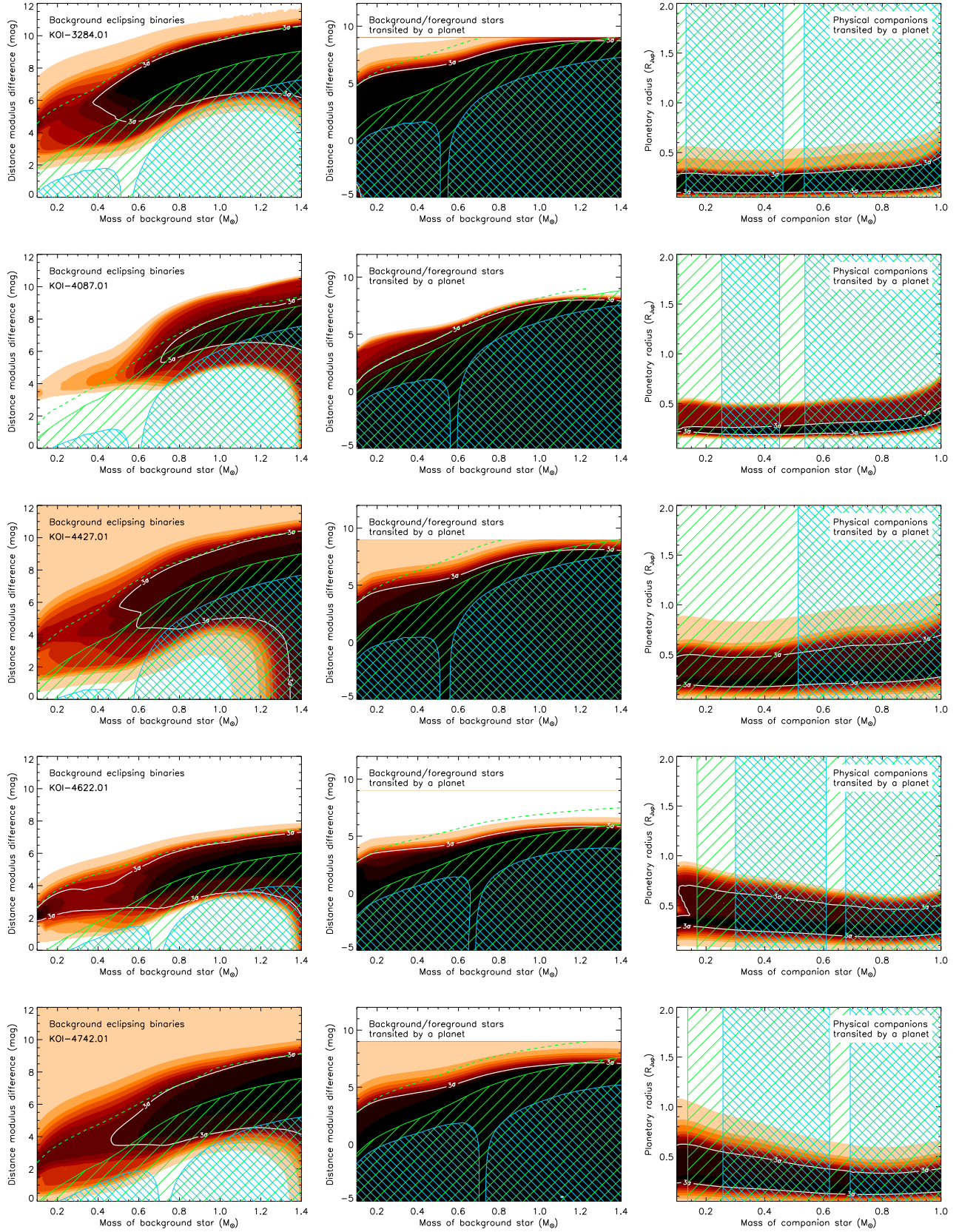


Figure 9. Same as Figure 8 for a second group of five KOIs in the sample.

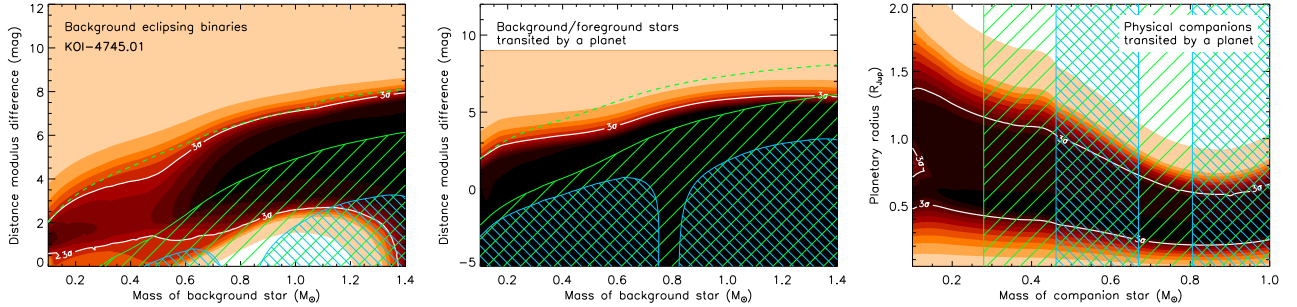


Figure 10. Same as Figure 8 for the remaining KOI in the sample.

duration), as they yield poor fits to the transit light curve. We also rejected configurations with companions bright enough that they would have been detected from our high-resolution imaging observations, our spectroscopic observations, by our centroid motion analysis, or that would yield an overall color for the blend inconsistent with the measured color of the target (Brown et al. 2011). In applying the spectroscopic constraint we excluded companions brighter than the limits described in Sect. 4.3 only if they are within $0''.43$ of the target (half width of the spectrometer slit), unless their radial velocity computed from the simulated orbit around the target is within 10 km s^{-1} of that of the primary. In that case, blending of the spectral lines of the secondary with those of the primary would prevent detection, so we considered those blends still viable. Finally, we retained only the false positive configurations that would be dynamically stable according to the criterion of Holman & Wiegert (1999). Since not every stellar companion will necessarily have a transiting planet and therefore act as a blend, as we assumed above, we adjusted the blend frequencies by accounting for the rate of occurrence of planets of each size and period as inferred from the KOI list itself. Minor corrections were applied to those rates for incompleteness and for the incidence of false positives in the KOI list, by means of simulations as described by Fressin et al. (2013). An additional adjustment was made to account for the dependence of the transit probability on the size of the secondary relative to the average size of the host stars in the KOI list. The final blend frequencies were obtained by multiplying by the occurrence rate of binary stars with planets as a function of binary semimajor axis, following Wang et al. (2014).

The calculation of the frequency of background or foreground stars transited by a planet (BP) proceeded in a similar fashion, and scales with the number density of stars in the vicinity of each target, for which we relied on predictions from the Galactic structure model of Robin et al. (2003, 2012) (Besançon model).²⁷ We gen-

erated a list of simulated stars in a 5 square-degree area around each of our targets, including their kinematic properties (radial velocity), and drew stars randomly from this list assigning them a random angular separation from the target within the corresponding 3σ exclusion region derived from our centroid motion analysis (since stars outside this area would have been detected; see Sect. 4.2). We assigned a random planet to each of these stars that we drew from the KOI list, keeping only those with orbital periods within a factor of two of that of the candidate, as done previously. False positive scenarios that do not meet the constraints from BLENDER were rejected, along with those that would have been flagged by our high-resolution imaging observations or color information. Further blends were excluded by the spectroscopic limits on the brightness of any unseen companions, as before, except for background/foreground stars whose spectral lines would be blended with those of the primary (i.e., those with simulated radial velocities within 10 km s^{-1} of the measured heliocentric velocity of the target), which we regarded as viable. Surviving blends were weighted by the corresponding rate of occurrence of transiting planets of that size and period, corrected as in the HTP case for incompleteness and false positives and adjusted for the dependence of the transit probability on the secondary radius. The final blend frequencies were then normalized by the ratio of the areas between the centroid exclusion region and 5 square degrees.

To estimate the frequency of BEBs acting as blends we again drew stars randomly from a list generated with the Besançon Galactic structure model, and paired them with an orbiting stellar companion (tertiary) generated from the distributions of binary properties by Raghavan et al. (2010) and Tokovinin (2014). We assigned orbital periods to these secondary-tertiary pairs drawn randomly from the catalog of *Kepler* eclipsing binaries of Slawson et al. (2011), retaining only those within a factor of two of the period of the candidate. Each blend was also assigned a random angular separation from the target within the 3σ exclusion limit from our centroid motion analysis. After rejecting scenarios that do not meet the constraints from BLENDER for acceptable fits to the transit light curve, we applied the

²⁷ We note that the current online version of the Besançon simulator (available at <http://model.obs-besancon.fr>) relies on stellar evolution models by Haywood (1994) to generate some of the stellar properties returned, including absolute magnitudes, colors, temperatures, and radii. Many of the simulated main-sequence stars of interest for our work are significantly cooler than the Sun (spectral type K and M), and the Haywood (1994) models are not specifically designed for such stars as they adopt gray boundary conditions and a rather simple equation of state, both of which result in increasingly biased predictions for cool stars (e.g., Chabrier et al. 2001). Because of this, we have preferred to recompute the relevant properties of all simulated stars adopting from the output of the

Besançon simulator only the basic characteristics that derive from the initial mass function and the Galactic structure model, which are the stellar mass, distance, age, and metallicity. We then used model isochrones from the Dartmouth series (Dotter et al. 2008) to generate all other stellar quantities for our purposes, as the physical ingredients of these isochrones give more realistic predictions for the lower main-sequence.

observational constraints (imaging, spectroscopy, color information) as in the BP scenario, and tallied the remaining viable blends. For computing the final BEB frequency, each surviving blend was assigned a weight given by the ratio of the eclipse probability of the particular blend (a function of the secondary and tertiary sizes) to the average eclipse probability for the Slawson et al. (2011) sample as a whole.

The probability that the candidate is a true planet as opposed to a false positive (‘planet prior’, PL) was estimated by simply counting the number of known KOIs with periods within a factor of two of each candidate, radii within 3σ of the measured planetary radius, and with similar transit durations. Incompleteness and false positive corrections were applied in the same way as above.

6.4. Results

Blend frequencies for the HTP, BP, and BEB scenarios are presented for each of our candidates in Table 7, along with the planet priors, PL. For the present work we have set a threshold for validation equivalent to a 3σ confidence level, consistent with previous applications of BLENDER. The statistical significance may be expressed as $PL/(PL + HTP + BP + BEB)$. For a 3σ validation we therefore require a planet prior that is at least $1/(1/99.73\% - 1) \approx 370$ times larger than the total blend frequency. We list these ‘odds ratios’ in Table 7, with the corresponding significance levels. For eleven of the twelve candidates we have achieved very robust validations at the 3σ level or higher, strongly supporting their true planetary nature. On this basis, the eight that have not been previously validated by others are given the new planet designations Kepler-436 b to Kepler-443 b (see Table 1). KOI-4427.01 has a lower odds ratio of only ~ 100 , corresponding to a significance level slightly over 99%. To avoid confusion in the rest of the paper we will continue to refer to the newly validated planets by their KOI numbers.

Strictly speaking, the above results compare the likelihood that the transit signals originate on the target itself with the likelihood that they come from eclipses associated with some other *unseen* star in the photometric aperture. However, four of our target stars (KOI-1422, 2529, 3255, and 3284) have *known* close companions from our high-resolution imaging observations, none of which can be ruled out as the source of the transit signal by our centroid motion analysis in Sect. 4.2. Thus, the possibility remains that the planets causing the signals orbit the companions rather than the targets. In that case, the inferred radius of the planets would be somewhat larger than the values derived in the next section, the exact amount depending on the brightness difference (dilution effect) and the physical size of the companion stars.

An estimate of the likelihood that the planets transit the companions was derived as follows. In each of the four cases we made the assumption that the companions are physically associated with the target. This is reasonable, as the probability of having an unrelated background star as close to the primary stars as observed is very small compared to that of a physical companion (see also Horch et al. 2014), based on the number density of stars around each KOI from the Besançon model and the known rate of occurrence of binaries (Raghavan et al.

2010; Wang et al. 2014). Furthermore, no signs of any of these companions are seen in our Keck/HIRES spectra even though in most cases they are bright enough to have been detected. This implies that their radial velocities must be similar to those of the primary stars so that the spectral lines are blended, preventing detection. This again argues for physical association.²⁸ In each case we then used the same isochrone as for the primaries to infer the companion properties, and we computed the ‘planet prior’ in the same way as for the targets, but this time assuming the planet transits the companion (i.e., increasing the dilution factor by the appropriate amount). We represent this planet prior for the companions as PL_{comp} , and we report these values in Table 7. Also given in the table are the probabilities that the planets transit the target rather than the companion, which we computed as $\mathcal{P}[\text{targ}] = PL/(PL + PL_{comp})$. For KOI-2529.02 the results allow us to state with high confidence that the planet orbits the target. For KOI-1422.04, KOI-1422.05, and KOI-3284.01 the calculations indicate a slight or modest preference for the planet being around the target rather than the companion, whereas for KOI-3255.01 the result is inconclusive. We return to this issue later in Sect. 8.3.

7. LIGHT CURVE FITS AND PLANETARY PARAMETERS

Having validated eleven of our candidates as bona-fide planets with very high confidence, and KOI-4427.01 to a lower degree of confidence, we subjected their light curves to a detailed modeling to infer the properties of the transiting objects. For this we used the detrended SAP time series from *Kepler* described earlier in Sect. 3. The transits were modeled using the standard Mandel & Agol (2002) algorithm employing the quadratic limb-darkening law. This simple model assumes a spherical, opaque planet transiting a spherically symmetric luminous star on a circular Keplerian orbit. We re-sampled the long-cadence data onto short-cadence sampling following the method described by Kipping (2010), to avoid smearing effects. Our model has eight free parameters in total. These are the orbital period, P , the time of transit center, τ , the planet-to-star radius ratio, R_p/R_* , the mean stellar density, $\rho_{*,\text{phot}}$, the impact parameter, b , the logarithm of fractional light contamination, $\log \beta$, and the quadratic limb-darkening coefficients q_1 and q_2 . All of these parameters have uniform priors in our fits, except $\rho_{*,\text{phot}}$, for which we employed a Jeffrey’s prior between 10^{-3} and 10^3 g cm^{-3} , and $\log \beta$, for which we used an informative Gaussian prior where appropriate.

In our model, β is the flux of any contaminating sources in the aperture divided by the flux of the target star. The purpose of this term is to account for dilution of the transit light curve due to close companions identified by the high spatial resolution imaging observations. We computed these ratios here based on the magnitude differences of the companions listed in Table 2, transformed to the Kp band, and assuming that all their flux is included in the aperture. For the wider companions (4–5'' separations) that are also in the aperture the transformed mag-

²⁸ In an independent study of KOI-1422, Star et al. (2014) also reached the conclusion that the companion is physically bound, based on numerical experiments with model isochrones.

Table 7
Blend frequencies, planet priors, odds ratios, and significance level of the validation for our targets.

Candidate	HTP	BP	BEB	PL	Odds ratio	Significance	PL_{comp}	$\mathcal{P}[\text{targ}]$
KOI-0571.05	1.15×10^{-6}	1.32×10^{-7}	6.60×10^{-8}	2.15×10^{-3}	1595	99.94%
KOI-1422.04	7.75×10^{-7}	4.74×10^{-8}	1.28×10^{-8}	3.19×10^{-4}	382	99.74%	5.94×10^{-4}	78.4%
KOI-1422.05	4.49×10^{-7}	4.84×10^{-8}	1.29×10^{-8}	4.63×10^{-4}	907	99.89%	7.25×10^{-5}	86.5%
KOI-2529.02	3.24×10^{-6}	2.17×10^{-9}	5.55×10^{-9}	1.31×10^{-3}	403	99.75%	5.61×10^{-6}	99.6%
KOI-3255.01	4.29×10^{-7}	4.79×10^{-11}	...	4.91×10^{-4}	1144	99.91%	4.39×10^{-4}	52.8%
KOI-3284.01	6.71×10^{-7}	1.10×10^{-9}	9.27×10^{-10}	1.57×10^{-3}	2333	99.96%	8.02×10^{-4}	66.2%
KOI-4005.01	3.71×10^{-7}	6.61×10^{-4}	1782	99.94%
KOI-4087.01	1.34×10^{-7}	1.32×10^{-4}	985	99.90%
KOI-4427.01	2.23×10^{-6}	1.07×10^{-9}	1.39×10^{-10}	2.62×10^{-4}	117	99.16%
KOI-4622.01	9.98×10^{-8}	3.82×10^{-10}	6.68×10^{-12}	2.08×10^{-3}	20761	99.99%
KOI-4742.01	1.37×10^{-6}	4.89×10^{-10}	5.45×10^{-12}	1.26×10^{-3}	919	99.89%
KOI-4745.01	1.53×10^{-6}	1.41×10^{-9}	9.19×10^{-12}	2.85×10^{-3}	1861	99.95%

Note. — For several of the candidates the blend frequencies for the BP and/or BEB scenarios are negligible and are not listed. For the four targets with close companions PL_{comp} is the planet prior assuming the planet transits the close companion, and $\mathcal{P}[\text{targ}]$ the probability that the planet transits the target rather than the companion.

nitudes were taken from the CFOP Web site, and for the closer ones we carried out the conversion using the Dartmouth isochrone for each target, on the assumption that the companions are physically associated. In the case of KOI-1422 we adopted the magnitude difference in the Kp band as reported by Star et al. (2014). The β factors range from 0.047 ± 0.009 for KOI-2529 to 0.83 ± 0.18 for KOI-3255, which has a very bright companion. Additionally, other nearby *Kepler* sources may contaminate the light curve (e.g., bleeding into the photometric aperture) and were corrected for using the reported contamination factors from the *Kepler* pipeline, treating them as fixed parameters.

It is worth noting that we did not directly fit for the standard quadratic limb darkening coefficients u_1 and u_2 , but instead we used the transformed parameters q_1 and q_2 as advocated by Kipping (2013b), in order to impose efficient, uninformative, and physical priors for the limb darkening profile. We note also that the out-of-transit baseline flux for each transit epoch was fitted as well. However, in this case we used a linear minimization to derive the baseline flux, similar to that described by Kundurthy et al. (2011). This treats the baseline flux simply as a nuisance parameter that is not marginalized against, but rather minimized at each Monte Carlo realization, reducing the number of free parameters yet at the same time allowing us to account for any residual offsets in the detrended light curves.

To regress our 8-parameter model to the observations, we employed the multi-modal nested sampling algorithm MULTINEST described by Feroz & Hobson (2008) and Feroz et al. (2009). We used 4000 live points with constant efficiency mode turned off, and set an enlargement factor of 0.1. The maximum *a posteriori* model parameters and their associated 68.3% credible intervals are collected in Tables 8 and 9. Also found there are other derived parameters including the scaled semimajor axis (a/R_*), the orbital inclination angle i , the transit durations T_{14} and T_{23} (first-to-fourth and second-to-third contacts), and the planetary radius and semimajor axis, R_p and a_p . Additional derived quantities of interest are discussed below. The folded transit light curves are displayed graphically in Figure 11 along with the models.

The planetary radii for our targets are all under $2.4 R_{\oplus}$

with the exception of KOI-2529.02, and the semimajor axes range from about 0.15 to 0.64 AU. We find that in all cases our planetary radii are larger than those currently held on the NASA Exoplanet Archive. This may be partly due to the fact that our stellar radii reported earlier also tend to be larger, and that in four cases we have included dilution effects from close companions.

[REST OF PAGE IS BLANK]

Table 8
Final parameter estimates for the objects studied in this work.

Parameter	KOI-0571.05	KOI-1422.04	KOI-1422.05	KOI-2529.02	KOI-3255.01	KOI-3284.01
Fitted parameters						
P [days]	129.9441 ^{+0.0013} _{-0.0012}	63.33600 ^{+0.00050} _{-0.00050}	34.14204 ^{+0.00025} _{-0.00029}	64.00205 ^{+0.00072} _{-0.00053}	66.65062 ^{+0.00033} _{-0.00032}	35.23319 ^{+0.00025} _{-0.00029}
τ [BJD _{UTC} - 2,400,000] ..	55789.4940 ^{+0.0036} _{-0.0041}	55692.3051 ^{+0.0026} _{-0.0026}	55686.0154 ^{+0.0030} _{-0.0035}	55477.6307 ^{+0.0042} _{-0.0049}	55670.6876 ^{+0.0023} _{-0.0023}	55673.0307 ^{+0.0044} _{-0.0032}
(R_p/R_*)	0.0205 ^{+0.0012} _{-0.0013}	0.0362 ^{+0.0022} _{-0.0018}	0.0297 ^{+0.0029} _{-0.0037}	0.0354 ^{+0.0024} _{-0.0035}	0.0279 ^{+0.0021} _{-0.0042}	0.0200 ^{+0.0020} _{-0.0018}
$\log(\rho_{\star, \text{phot}} [\text{g cm}^{-3}])^{\text{a}}$	0.80 ^{+0.40} _{-0.17}	1.08 ^{+0.29} _{-0.15}	0.77 ^{+0.44} _{-0.19}	0.72 ^{+0.36} _{-0.21}	0.50 ^{+0.19} _{-0.19}	0.78 ^{+0.38} _{-0.28}
b	0.13 ^{+0.28} _{-0.13}	0.09 ^{+0.26} _{-0.09}	0.18 ^{+0.30} _{-0.18}	0.09 ^{+0.29} _{-0.09}	0.56 ^{+0.30} _{-0.31}	0.90 ^{+0.08} _{-0.34}
q_1	0.35 ^{+0.31} _{-0.28}	0.03 ^{+0.16} _{-0.03}	0.93 ^{+0.07} _{-0.18}	0.21 ^{+0.32} _{-0.21}	0.36 ^{+0.26} _{-0.36}	0.85 ^{+0.15} _{-0.30}
q_2	0.08 ^{+0.27} _{-0.08}	0.03 ^{+0.22} _{-0.03}	0.97 ^{+0.03} _{-0.15}	0.05 ^{+0.30} _{-0.05}	0.39 ^{+0.30} _{-0.30}	0.54 ^{+0.32} _{-0.34}
$\log \beta$	$(-0.532 \pm 0.089)^{\text{b}}$	$(-0.532 \pm 0.089)^{\text{b}}$	$(-1.330 \pm 0.084)^{\text{b}}$	$(-0.080 \pm 0.089)^{\text{b}}$	$(-0.577 \pm 0.070)^{\text{b}}$
Other transit parameters						
(a/R_*)	178 ⁺⁶⁵ ₋₂₁	137 ⁺³⁴ ₋₁₅	71 ⁺²⁹ ₋₁₀	104 ⁺³⁴ ₋₁₆	91 ⁺¹⁴ ₋₁₂	73 ⁺²⁶ ₋₁₅
i [°]	89.96 ^{+0.04} _{-0.10}	89.95 ^{+0.05} _{-0.12}	89.89 ^{+0.11} _{-0.26}	89.93 ^{+0.07} _{-0.18}	89.90 ^{+0.10} _{-0.23}	89.86 ^{+0.14} _{-0.32}
u_1	0.70 ^{+0.39} _{-0.38}	0.35 ^{+0.31} _{-0.32}	1.52 ^{+0.32} _{-0.34}	0.67 ^{+0.44} _{-0.48}	0.92 ^{+0.35} _{-0.31}	0.88 ^{+0.47} _{-0.51}
u_2	-0.16 ^{+0.31} _{-0.30}	-0.01 ^{+0.35} _{-0.20}	-0.70 ^{+0.23} _{-0.27}	-0.14 ^{+0.38} _{-0.31}	-0.31 ^{+0.25} _{-0.33}	-0.42 ^{+0.32} _{-0.56}
T_{14} [hours]	5.62 ^{+0.34} _{-0.24}	3.60 ^{+0.19} _{-0.18}	3.62 ^{+0.26} _{-0.26}	4.67 ^{+0.35} _{-0.34}	5.59 ^{+0.21} _{-0.29}	3.48 ^{+0.30} _{-0.41}
T_{23} [hours]	5.22 ^{+0.25} _{-0.30}	3.26 ^{+0.19} _{-0.19}	3.34 ^{+0.31} _{-0.26}	4.16 ^{+0.33} _{-0.43}	5.21 ^{+0.27} _{-0.24}	3.24 ^{+0.31} _{-0.39}
Physical parameters						
$R_p [R_{\oplus}]$	1.17 ^{+0.08} _{-0.08}	1.75 ^{+0.12} _{-0.19}	1.48 ^{+0.16} _{-0.25}	2.73 ^{+0.23} _{-0.24}	2.14 ^{+0.22} _{-0.17}	1.12 ^{+0.16} _{-0.17}
a_p [AU]	0.432 ^{+0.171} _{-0.053}	0.283 ^{+0.046} _{-0.041}	0.149 ^{+0.035} _{-0.024}	0.339 ^{+0.134} _{-0.053}	0.288 ^{+0.066} _{-0.040}	0.166 ^{+0.051} _{-0.042}
$\log(\rho_{\star} [\text{g cm}^{-3}])^{\text{c}}$	0.734 ^{+0.022} _{-0.020}	0.915 ^{+0.069} _{-0.064}	0.915 ^{+0.069} _{-0.064}	0.482 ^{+0.036} _{-0.036}	0.504 ^{+0.035} _{-0.035}	0.717 ^{+0.079} _{-0.156}
e_{min}	0.04 ^{+0.07} _{-0.04}	0.12 ^{+0.10} _{-0.09}	0.10 ^{+0.14} _{-0.10}	0.19 ^{+0.13} _{-0.11}	0.02 ^{+0.08} _{-0.02}	0.03 ^{+0.10} _{-0.03}
$S_{\text{eff}} [S_{\oplus}]$	0.30 ^{+0.10} _{-0.15}	0.39 ^{+0.10} _{-0.16}	1.45 ^{+0.50} _{-0.73}	1.69 ^{+0.58} _{-0.79}	2.15 ^{+0.74} _{-0.88}	1.40 ^{+0.67} _{-0.77}
$\mathcal{P}[\text{HZ}]$ [%]	98.4	99.7	82.0	72.3	56.8	71.8
$\mathcal{P}[\text{rocky}]$ [%]	68.4	30.6	50.7	0.6	11.7	69.6

Note. — All quantities correspond to the mode of the posterior distributions.

^a Mean stellar density derived from the light curve fit.

^b Gaussian prior.

^c Mean stellar density derived from our stellar evolution modeling.

Table 9
Final parameter estimates for the objects studied in this work.

Parameter	KOI-4005.01	KOI-4087.01	KOI-4427.01	KOI-4622.01	KOI-4742.01	KOI-4745.01
Fitted parameters						
P [days]	178.1396 ^{+0.0016} _{-0.0018}	101.11141 ^{+0.00087} _{-0.00068}	147.6606 ^{+0.0011} _{-0.0014}	207.2482 ^{+0.0022} _{-0.0020}	112.3053 ^{+0.0024} _{-0.0028}	177.6693 ^{+0.0031} _{-0.0030}
τ [BJD _{UTC} - 2,400,000] ..	55399.3987 ^{+0.0039} _{-0.0054}	55756.2986 ^{+0.0028} _{-0.0027}	55815.2616 ^{+0.0047} _{-0.0042}	55667.7764 ^{+0.0040} _{-0.0065}	55849.5578 ^{+0.0067} _{-0.0056}	55630.2460 ^{+0.0076} _{-0.0077}
(R_p/R_*)	0.02392 ^{+0.00099} _{-0.00111}	0.03038 ^{+0.00112} _{-0.00098}	0.0339 ^{+0.0022} _{-0.0020}	0.0280 ^{+0.0017} _{-0.0014}	0.0211 ^{+0.0019} _{-0.0016}	0.0304 ^{+0.0022} _{-0.0022}
$\log(\rho_{\star, \text{phot}} [\text{g cm}^{-3}])^{\text{a}}$	0.23 ^{+0.16} _{-0.15}	0.25 ^{+0.13} _{-0.13}	0.78 ^{+0.36} _{-0.14}	0.89 ^{+0.36} _{-0.16}	0.68 ^{+0.56} _{-0.20}	0.32 ^{+0.30} _{-0.20}
b	0.10 ^{+0.28} _{-0.10}	0.09 ^{+0.27} _{-0.09}	0.08 ^{+0.25} _{-0.08}	0.25 ^{+0.30} _{-0.25}	0.22 ^{+0.29} _{-0.22}	0.26 ^{+0.32} _{-0.26}
q_1	0.05 ^{+0.16} _{-0.05}	0.03 ^{+0.10} _{-0.03}	0.16 ^{+0.26} _{-0.16}	0.03 ^{+0.15} _{-0.03}	0.92 ^{+0.08} _{-0.31}	0.33 ^{+0.32} _{-0.33}
q_2	0.08 ^{+0.24} _{-0.08}	0.03 ^{+0.20} _{-0.03}	0.08 ^{+0.30} _{-0.08}	0.03 ^{+0.21} _{-0.03}	0.90 ^{+0.10} _{-0.30}	0.12 ^{+0.29} _{-0.12}
$\log \beta$	$(-0.804 \pm 0.089)^{\text{b}}$
Other transit parameters						
(a/R_*)	142 ⁺¹⁸ ₋₁₅	99.0 ^{+10.2} _{-9.4}	190 ⁺⁶² ₋₂₁	260 ⁺⁸³ ₋₃₁	146 ⁺⁸⁰ ₋₂₂	151 ⁺³⁹ ₋₂₂
i [°]	89.95 ^{+0.05} _{-0.12}	89.93 ^{+0.07} _{-0.18}	89.97 ^{+0.03} _{-0.08}	89.97 ^{+0.03} _{-0.07}	89.94 ^{+0.06} _{-0.12}	89.94 ^{+0.06} _{-0.13}
u_1	0.39 ^{+0.28} _{-0.34}	0.34 ^{+0.24} _{-0.23}	0.67 ^{+0.41} _{-0.39}	0.28 ^{+0.27} _{-0.28}	1.03 ^{+0.50} _{-0.49}	0.65 ^{+0.41} _{-0.48}
u_2	-0.08 ^{+0.25} _{-0.23}	-0.05 ^{+0.21} _{-0.19}	-0.23 ^{+0.26} _{-0.34}	-0.02 ^{+0.30} _{-0.20}	-0.43 ^{+0.32} _{-0.43}	-0.15 ^{+0.25} _{-0.31}
T_{14} [hours]	9.59 ^{+0.30} _{-0.42}	7.95 ^{+0.25} _{-0.21}	5.99 ^{+0.33} _{-0.29}	6.05 ^{+0.30} _{-0.32}	5.62 ^{+0.40} _{-0.52}	8.95 ^{+0.54} _{-0.59}
T_{23} [hours]	9.04 ^{+0.36} _{-0.35}	7.27 ^{+0.23} _{-0.33}	5.42 ^{+0.28} _{-0.37}	5.61 ^{+0.30} _{-0.32}	5.26 ^{+0.40} _{-0.52}	8.28 ^{+0.70} _{-0.56}
Physical parameters						
$R_p [R_{\oplus}]$	2.24 ^{+0.16} _{-0.45}	1.86 ^{+0.24} _{-0.19}	1.84 ^{+0.22} _{-0.24}	1.64 ^{+0.22} _{-0.24}	1.34 ^{+0.11} _{-0.18}	2.33 ^{+0.19} _{-0.22}
a_p [AU]	0.563 ^{+0.165} _{-0.080}	0.242 ^{+0.066} _{-0.041}	0.419 ^{+0.073} _{-0.081}	0.64 ^{+0.32} _{-0.13}	0.409 ^{+0.209} _{-0.060}	0.495 ^{+0.186} _{-0.075}
$\log(\rho_{\star} [\text{g cm}^{-3}])^{\text{c}}$	0.295 ^{+0.084} _{-0.076}	0.657 ^{+0.084} _{-0.162}	0.751 ^{+0.083} _{-0.095}	0.672 ^{+0.091} _{-0.211}	0.605 ^{+0.036} _{-0.035}	0.477 ^{+0.043} _{-0.035}
e_{min}	0.03 ^{+0.08} _{-0.03}	0.34 ^{+0.12} _{-0.19}	0.02 ^{+0.07} _{-0.02}	0.10 ^{+0.11} _{-0.10}	0.04 ^{+0.08} _{-0.04}	0.11 ^{+0.15} _{-0.11}
$S_{\text{eff}} [S_{\oplus}]$	1.83 ^{+0.51} _{-0.62}	1.20 ^{+0.46} _{-0.65}	0.233 ^{+0.069} _{-0.110}	0.21 ^{+0.11} _{-0.11}	0.66 ^{+0.23} _{-0.41}	0.86 ^{+0.29} _{-0.37}
$\mathcal{P}[\text{HZ}]$ [%]	74.1	89.0	71.9	48.6	96.9	89.9
$\mathcal{P}[\text{rocky}]$ [%]	6.5	29.8	27.3	45.0	60.7	4.9

Note. — All quantities correspond to the mode of the posterior distributions.

^a Mean stellar density derived from the light curve fit.

^b Gaussian prior.

^c Mean stellar density derived from our stellar evolution modeling.

8. CONSTRAINTS FROM ASTERODENSITY PROFILING

A comparison between the mean stellar density inferred from our light-curve fits above (photometric density $\rho_{\star,\text{phot}}$) and some independent measure of the density, such as that derived from model isochrones, can provide very useful information about a planetary system. This technique, referred to as Asterodensity Profiling (AP), was discussed in detail by Kipping et al. (2012).²⁹ For a “vanilla” exoplanet (circular Keplerian orbit, no blends, etc.) these two density metrics should agree. Deviations between them occur when one of the following physical effects is not accounted for in the light curve analysis: *i*) orbital eccentricity (‘photo-eccentric effect’); *ii*) contaminating light (‘photo-blend effect’); *iii*) unocculted star spots (‘photo-spot effect’); *iv*) transit timing variations (‘photo-timing effect’); *v*) transit duration variations (‘photo-duration effect’); *vi*) substantial mass of the transiting object (‘photo-mass effect’); or *vii*) the object orbits a different star. These effects have been described in detail by Kipping (2014a), who provided approximate expressions for each.

In what follows we apply AP to 1) test the hypothesis that all planets in the multiple transiting planet systems KOI-0571 and KOI-1422 orbit the same star (Multi-body Asterodensity Profiling, or MAP; Kipping et al. 2012); 2) derive minimum eccentricities for the twelve KOIs in our sample; and 3) evaluate the possibility that the validated planet orbits the close companion instead of the target, in the four cases where high-resolution imaging has identified such sources.

8.1. Using AP to derive average stellar densities for the multi-planet systems KOI-0571 and KOI-1422

Of the twelve candidates studied in this work, three reside in systems with five transiting planets each: one orbits KOI-0571, and two are associated with KOI-1422. These rare systems provide extra information that we will exploit here. For each planetary candidate in each system we performed an independent detrending and subsequent light curve fit using the methods described earlier.

If all five planets in each of these two systems orbit the same star, then we expect all of the planets to maintain low orbital eccentricities in order for these compact systems to be dynamically stable over Gyr timescales (see also Rowe et al. 2014). Therefore, under the assumption that the planets orbit the same star, one would expect negligible photo-eccentric effects, implying that the mean stellar densities derived from the light curves should be consistent. On the same assumption that all five planets orbit the same star, two other AP effects listed above can also be neglected: the photo-blend effect, and effects from the planets orbiting different stars. The latter scenario is obviously not relevant under the posed assumption, and the former can be negated since, to first order, contaminating light that is unaccounted for disturbs the light-curve-derived stellar density for all five planets to the same degree.

A comparison of the photometric stellar densities for the five planets around KOI-0571 and KOI-1422 reveals

excellent agreement in both cases, as shown in Figure 12. Furthermore, similar diagrams (not shown) comparing the limb-darkening parameters u_1 and u_2 also show very good agreement among all planets in both systems. We conclude from this that each system is consistent with having five planets orbiting the same star, given the available data.

Averaging over the four other planets in KOI-0571, and the three others in KOI-1422, we may derive a mean photometric density for the host stars that we denote $\rho_{\star,\text{MAP}}$. We obtained $\rho_{\star,\text{MAP}} = 5.41^{+0.32}_{-0.24} \text{ g cm}^{-3}$ and $7.2^{+2.9}_{-1.2} \text{ g cm}^{-3}$, respectively, where the extra dilution from the close companion to KOI-1422 has been properly accounted for, as before. The 1σ and 2σ confidence intervals of these values are marked in Figure 12 with dashed lines. Both of these mean densities are consistent with the corresponding photometric densities derived from the light curves of KOI-0571.05, KOI-1422.04, and KOI-1422.05 individually, which are $\rho_{\star,\text{phot}} = 5.9^{+1.4}_{-2.5} \text{ g cm}^{-3}$, $11.4^{+7.5}_{-4.0} \text{ g cm}^{-3}$, and $5.3^{+2.7}_{-2.4} \text{ g cm}^{-3}$, respectively.

The average stellar densities for these multi-planet systems (computed from the remaining planets in each case, excluding the validated planets) were used as luminosity indicators to strengthen the determination of the host star parameters via our stellar evolution modeling in Sect. 5 (Sozzetti et al. 2007). This is particularly useful for these three KOIs as neither of the host stars has a spectroscopic determination of $\log g$ available to otherwise constrain the luminosity (see Table 5).

8.2. Using AP to measure minimum eccentricities

A measure of the stellar density that is independent of that derived from the individual light curves of the validated planets is available for each of the twelve KOIs studied in this work (see Sect. 5). For KOI-0571 and KOI-1422, this comes from the MAP-based density ($\rho_{\star,\text{MAP}}$) refined by our isochrone analysis by making use of additional constraints on age from gyrochronology, along with the spectroscopic temperature and metallicity estimates. For KOI-3284, 4087, 4427, and 4622 our stellar evolution modeling used only the age along with T_{eff} and $[\text{Fe}/\text{H}]$, and for the remaining targets that are earlier in spectral type we used $\log g$ as the luminosity indicator, which for these stars we were able to determine spectroscopically using *SpecMatch*.

These independent stellar densities, denoted here simply by ρ_{\star} , may be compared with the light-curve-derived stellar density of each validated planet, $\rho_{\star,\text{phot}}$. In these cases we expect the photo-eccentric effect to be the dominant AP effect since contamination has been accounted for in the fits (photo-blend effect), the stars show relatively low activity (photo-spot effect), there are no known timing effects for these objects (photo-timing and photo-duration effects), and their small sizes suggest they should be of low mass (photo-mass effect). We therefore attribute any differences between $\rho_{\star,\text{phot}}$ and ρ_{\star} as being due to orbital eccentricity. The minimum eccentricity for each KOI is directly given by this comparison via the expression presented by Kipping (2014a),

$$e_{\text{min}} = \frac{|1 - (\rho_{\star,\text{phot}}/\rho_{\star})^{2/3}|}{1 + (\rho_{\star,\text{phot}}/\rho_{\star})^{2/3}}.$$

²⁹ A similar concept was described by Tingley et al. (2011), although the current implementation is considerably more advanced.

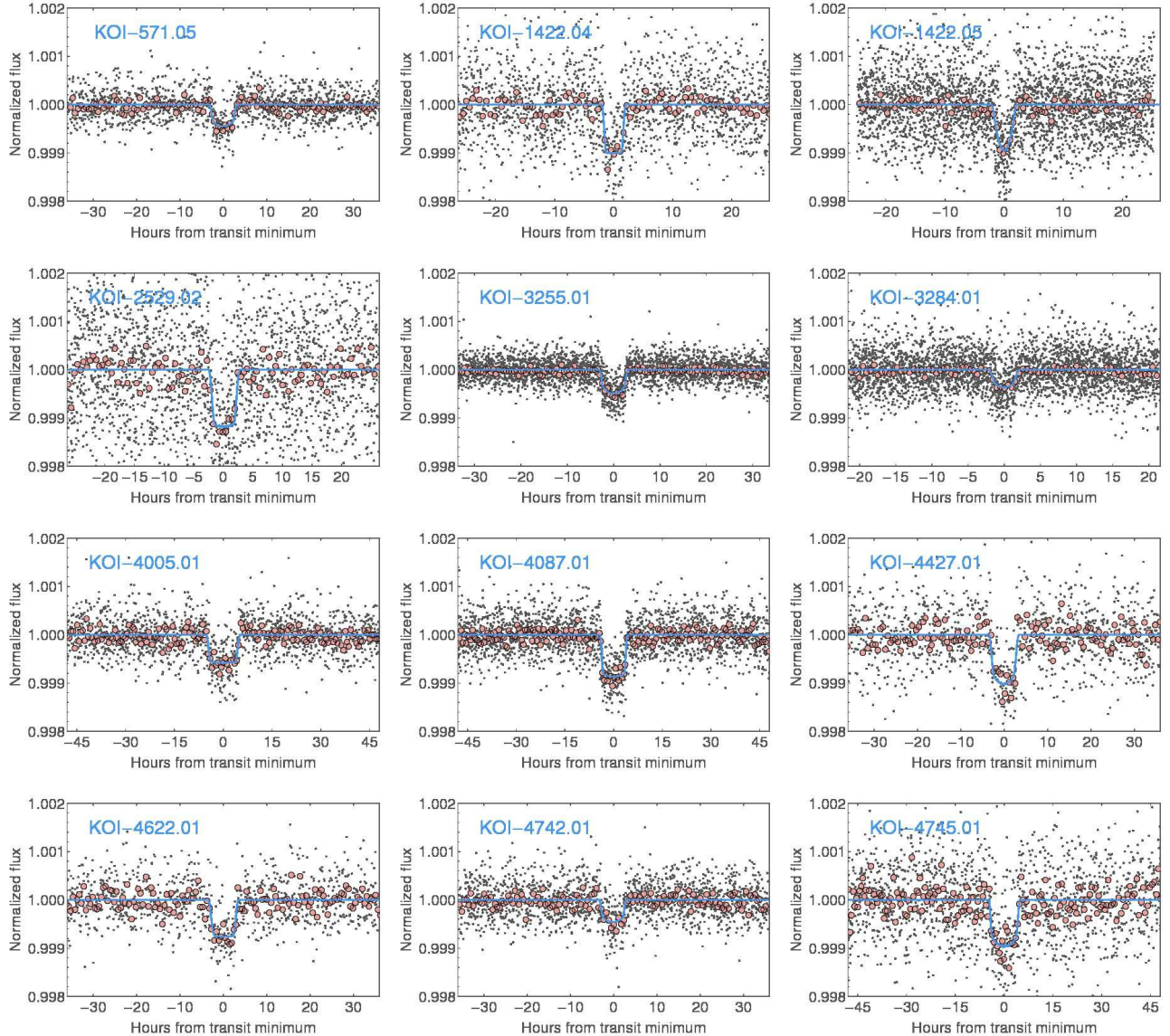


Figure 11. Light curve fits and *Kepler* observations (small dots) for our twelve KOIs. Pink circles represent 10-point binned data.

The results of this calculation, shown in Tables 8 and 9, reveal that most of the KOIs in the sample are consistent with orbiting their parent stars on low-eccentricity orbits.

8.3. Using AP to test blend scenarios

For the four KOIs found to have close companions from our high-resolution imaging (KOI-1422, 2529, 3255, and 3284) the same techniques from the preceding section enable us to revisit the possibility that the planets orbit the companions rather than the primary stars. As done earlier, we made the reasonable assumption that these close neighbors are bound to the targets. This allows us to reuse the target isochrones to infer approximate stellar properties for the companions, including their mean densities, on the basis of their brightness differences compared to the target. We re-fitted the transits adopting revised blend factors (β) appropriate for the different host stars to derive photometric densities for the companions, $\rho_{\star, \text{phot}}$. We then used these densities to estimate a minimum eccentricity for the scenarios in which the planets

orbit the companions rather than the brighter stars.

We report the results of this calculation in Table 10, where we list also the planetary radii that we infer if the planets transited the companions, as well as their effective insolation level (see next section). Although the eccentricity distribution of small planets around M dwarf stars is presently unknown (Kipping 2014b), in general we expect circular orbits to be more likely than eccentric orbits, based on evidence from other sub-populations of planets (see, e.g., Kipping 2013a). We may thus use e_{min} as a rough criterion to decide which location for the planet is favored. Additionally, the sign of the quantity $\log(\rho_{\star, \text{phot}}/\rho_{\star})$ conveys useful information. From geometric arguments, a planet in an eccentric orbit has a higher probability of transiting near periapsis than apoapsis (e.g., Barnes 2007). For the more probable case of $0 < \omega < \pi$ (“near” periapsis transits), one expects $\log(\rho_{\star, \text{phot}}/\rho_{\star}) > 0$. In contrast, for the less probable scenario of $\pi < \omega < 2\pi$ (“near” apoapsis transits), one expects $\log(\rho_{\star, \text{phot}}/\rho_{\star}) < 0$ (see Kipping 2014a). There-

Table 10
AP-derived minimum eccentricities and other properties for
KOIs with close companions.

Parameter	Primary	Companion
KOI-1422.04		
Kp [mag].....	16.15 ± 0.03	17.72 ± 0.15
$\log \beta$	(-0.628 ± 0.061)	(0.628 ± 0.061)
$\log(\rho_\star [\text{g cm}^{-3}])$	$0.915^{+0.069}_{-0.064}$	$1.342^{+0.037}_{-0.036}$
$\log(\rho_{\star,\text{phot}} [\text{g cm}^{-3}])$..	$1.08^{+0.29}_{-0.15}$	$1.08^{+0.27}_{-0.13}$
$\log(\rho_{\star,\text{phot}}/\rho_\star)$	$0.16^{+0.37}_{-0.17}$	$-0.27^{+0.34}_{-0.14}$
e_{\min}	$0.12^{+0.10}_{-0.09}$	$0.20^{+0.10}_{-0.20}$
$R_p [R_\oplus]$	$1.76^{+0.16}_{-0.14}$	$2.01^{+0.18}_{-0.18}$
$S_{\text{eff}} [S_\oplus]$	$0.38^{+0.11}_{-0.16}$	$0.28^{+0.06}_{-0.10}$
KOI-1422.05		
Kp [mag].....	16.15 ± 0.03	17.72 ± 0.15
$\log \beta$	(-0.628 ± 0.061)	(0.628 ± 0.061)
$\log(\rho_\star [\text{g cm}^{-3}])$	$0.915^{+0.069}_{-0.064}$	$1.342^{+0.037}_{-0.036}$
$\log(\rho_{\star,\text{phot}} [\text{g cm}^{-3}])$..	$0.77^{+0.44}_{-0.19}$	$0.77^{+0.43}_{-0.28}$
$\log(\rho_{\star,\text{phot}}/\rho_\star)$	$-0.14^{+0.58}_{-0.21}$	$-0.56^{+0.42}_{-0.27}$
e_{\min}	$0.10^{+0.14}_{-0.10}$	$0.79^{+0.05}_{-0.22}$
$R_p [R_\oplus]$	$1.42^{+0.19}_{-0.18}$	$1.68^{+0.27}_{-0.53}$
$S_{\text{eff}} [S_\oplus]$	$1.35^{+0.49}_{-0.66}$	$1.01^{+0.50}_{-0.47}$
KOI-2529.02		
Kp [mag].....	15.86 ± 0.10	22.00 ± 0.20
$\log \beta$	(-1.330 ± 0.084)	(2.474 ± 0.089)
$\log(\rho_\star [\text{g cm}^{-3}])$	$0.482^{+0.036}_{-0.036}$	$1.866^{+0.046}_{-0.039}$
$\log(\rho_{\star,\text{phot}} [\text{g cm}^{-3}])$..	$0.72^{+0.36}_{-0.21}$	$0.88^{+0.14}_{-0.13}$
$\log(\rho_{\star,\text{phot}}/\rho_\star)$	$0.24^{+0.40}_{-0.21}$	$-1.01^{+0.13}_{-0.15}$
e_{\min}	$0.19^{+0.13}_{-0.11}$	$0.65^{+0.06}_{-0.06}$
$R_p [R_\oplus]$	$2.73^{+0.23}_{-0.24}$	$8.2^{+2.1}_{-2.8}$
$S_{\text{eff}} [S_\oplus]$	$1.69^{+0.58}_{-0.79}$	$0.30^{+0.06}_{-0.08}$
KOI-3255.01		
Kp [mag].....	15.01 ± 0.10	15.21 ± 0.20
$\log \beta$	(-0.080 ± 0.089)	(0.080 ± 0.089)
$\log(\rho_\star [\text{g cm}^{-3}])$	$0.504^{+0.035}_{-0.035}$	$0.524^{+0.009}_{-0.010}$
$\log(\rho_{\star,\text{phot}} [\text{g cm}^{-3}])$..	$0.50^{+0.19}_{-0.19}$	$0.51^{+0.16}_{-0.18}$
$\log(\rho_{\star,\text{phot}}/\rho_\star)$	$0.01^{+0.22}_{-0.18}$	$0.00^{+0.17}_{-0.16}$
e_{\min}	$0.02^{+0.08}_{-0.02}$	$0.02^{+0.08}_{-0.02}$
$R_p [R_\oplus]$	$2.14^{+0.22}_{-0.17}$	$2.25^{+0.20}_{-0.20}$
$S_{\text{eff}} [S_\oplus]$	$2.15^{+0.74}_{-0.88}$	$1.91^{+0.57}_{-0.49}$
KOI-3284.01		
Kp [mag].....	14.58 ± 0.10	17.01 ± 0.20
$\log \beta$	(-0.577 ± 0.070)	(1.036 ± 0.088)
$\log(\rho_\star [\text{g cm}^{-3}])$	$0.717^{+0.079}_{-0.156}$	$1.321^{+0.020}_{-0.011}$
$\log(\rho_{\star,\text{phot}} [\text{g cm}^{-3}])$..	$0.78^{+0.38}_{-0.28}$	$0.77^{+0.43}_{-0.28}$
$\log(\rho_{\star,\text{phot}}/\rho_\star)$	$-0.03^{+0.31}_{-0.35}$	$-0.54^{+0.42}_{-0.27}$
e_{\min}	$0.03^{+0.10}_{-0.03}$	$0.40^{+0.16}_{-0.31}$
$R_p [R_\oplus]$	$1.12^{+0.16}_{-0.17}$	$1.77^{+0.23}_{-0.21}$
$S_{\text{eff}} [S_\oplus]$	$1.40^{+0.67}_{-0.77}$	$0.86^{+0.39}_{-0.39}$

Note. — The $\log \beta$ values indicated in parentheses were used as Gaussian priors. For KOI-2529.02 and KOI-3284.01 the β factors for the companions are not the reciprocal of the values for the primaries because of the presence of additional companions in the aperture (see Table 2). Those additional stars are ruled out as the source of the transit signals by our centroid analysis of Sect. 4.2, but still cause dilution. The symbol ρ_\star represents the mean stellar density based on our isochrone analysis (and other constraints), while $\rho_{\star,\text{phot}}$ is the photometric density from the individual light curve fit for the planet.

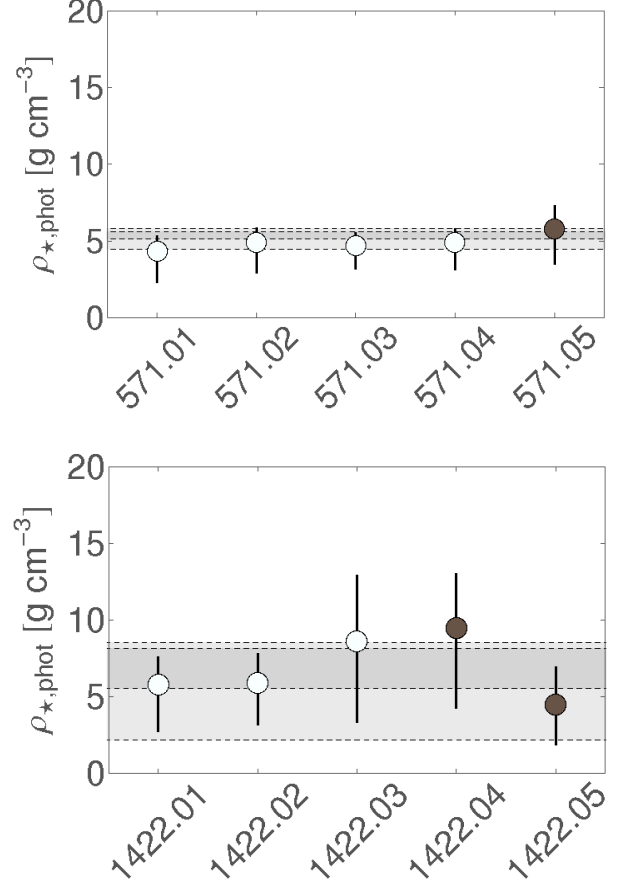


Figure 12. Mean stellar densities from separate light curve fits to each of the planets in the five-planet systems KOI-0571 and 1422. The dashed lines and gray areas represent the 1σ and 2σ confidence regions of the average density computed from the other companions in each system (open circles) excluding the ones we have validated here (filled circles). In both cases the agreement between this mean density and the separately determined one of the validated planets is excellent, supporting the notion that in each system all five planets orbit the same star.

fore, in general the photo-eccentric effect is more likely to (but will not necessarily) produce a positive sign for this logarithmic ratio. Additionally, a diluted transit in a circular orbit will cause $\log(\rho_{\star,\text{phot}}/\rho_\star)$ to be negative via the photo-blend effect (Kipping 2014a), but can never yield a positive sign. For these reasons, finding $\log(\rho_{\star,\text{phot}}/\rho_\star) > 0$ is more consistent with a bona-fide planet than a negative sign.

As seen in Table 10, despite the large uncertainties the minimum eccentricities are considerably higher if KOI-1422.05, KOI-2529.02 and KOI-3284.01 orbit the secondary star, which seems *a priori* less likely, although quantifying an accurate odds ratio is not possible without knowing the eccentricity distribution of terrestrial-sized planets around M dwarfs. For the first two cases this assessment agrees with our conclusion from the BLENDER study (Table 7), which also favored the planet transiting the primary. For KOI-2529.02 and KOI-3284.01 the sign of the log-density ratio $\log(\rho_{\star,\text{phot}}/\rho_\star)$ is also negative if the planet is around the companion, requiring either geometrically disfavored near-apoapsis transiting planets, or simply the photo-blend effect. For KOI-1422.04 the minimum eccentricities between the two scenarios are

comparable, but the sign of the log-density ratio favors the primary star as the host. Finally, the test for KOI-3255.01 is ambiguous according to both metrics, in agreement with the indications from BLENDER that were also inconclusive for this planet.

9. HABITABILITY

While a broadband transit light curve alone does not reveal the “habitability” of a given planet, it does allow us to determine how close to the “habitable zone” a particular planet is. Therefore, an important distinction to make is that we do not claim any of the planets in our sample are truly habitable, but merely that the insolation they receive from the host star is suitable for the presence of liquid water on the surface across the range of plausible atmospheric conditions.

Kopparapu et al. (2013) have presented calculations of the habitable zone for a wide variety of atmospheric conditions, and considered also empirical boundaries for the hot inner edge modeled by a recent-Venus-like world, and a cold outer edge modeled by an early-Mars-like world. More recently Zsom et al. (2013) took a broader view of the conditions that might provide habitable surface conditions closer to the host star, and postulated an inner boundary for the HZ that can be as close as 0.38 AU for a solar-type star if the relative humidity of the planetary atmosphere is low and the albedo high. Given the complexity of the problem and our still limited state of knowledge, in this work we have chosen to adopt the broadest possible limits that can plausibly lead to suitable conditions for life, in order to avoid prematurely dismissing as uninteresting planets that may yet be habitable. Specifically, we adopted the empirical cold outer boundary for the HZ of Kopparapu et al. (2013) modeled by an early-Mars-like world, and the inner edge for dry desert worlds from Zsom et al. (2013). These boundaries depend upon two key input parameters: S_{eff} , the effective insolation received by the planet, and the spectral type of the star, for which the usual proxy is T_{eff} , the star’s effective temperature. We define S_{eff} in terms of the Earth’s insolation, S_{\oplus} , as

$$\frac{S_{\text{eff}}}{S_{\oplus}} = \frac{L_{\star}/L_{\odot}}{(a_p/\text{AU})^2 \sqrt{1-e^2}},$$

where L_{\star} is the stellar luminosity and a_p the planetary semimajor axis in astronomical units. For each planet in our sample we computed a joint posterior for S_{eff} and T_{eff} based on the stellar properties inferred in Sect. 5, assuming the planet’s orbit is circular. At each realization in this posterior we evaluated whether the sample falls inside or outside the adopted HZ boundaries. Counting the total number of cases inside allows us to assign a statistical confidence that the planet in question is in the HZ, denoted $\mathcal{P}[\text{HZ}]$. We provide those results in Tables 8 and 9. This statistical approach to the habitable zone was first described by Kipping et al. (2013) for the planet Kepler-22 b.

Additionally, we consider the radius of the planet to be an important parameter in assessing its potential for habitability, as this can determine whether the planet is likely to have a solid surface that can support liquid water. In the past it was often conventionally assumed that there likely existed

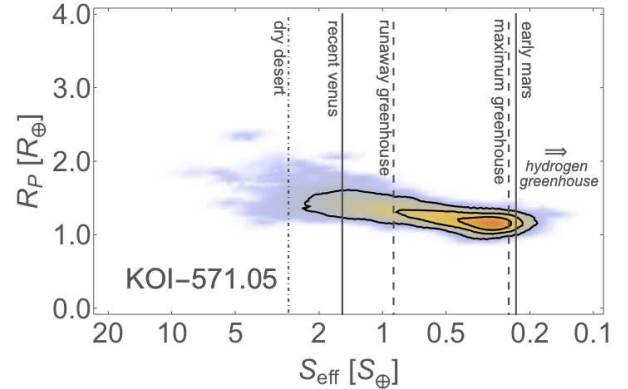


Figure 13. Joint posterior distribution of the planetary radius (y axis) and effective insolation (x axis) for KOI-0571.05 (Kepler-186 f). Labeled vertical lines mark the various boundaries of the habitable zone as defined by Kopparapu et al. (2013) and Zsom et al. (2013). Here we adopt the optimistic ‘dry desert’ and ‘early Mars’ inner and outer edges, respectively. These lines are drawn assuming an effective stellar temperature equal to the mode of the associated posteriors. Contours enclose 68.3%, 95.4% and 99.7% of the Monte Carlo samples (corresponding to the 1σ , 2σ , and 3σ levels).

some boundary in radius between rocky planets and mini-Neptunes (e.g., Weiss et al. 2013), perhaps around $1.75 R_{\oplus}$ (Lopez & Fortney 2013). However, recent counter-examples to this paradigm make such a simplistic division questionable. For example, KOI-314 c is a mini-Neptune despite being $1.6 R_{\oplus}$ (Kipping et al. 2014a), and Kepler-10 c has been claimed to be rocky despite being $2.35 R_{\oplus}$ (Dumusque et al. 2014; for a differing view see Rogers 2014 and Wolfgang & Lopez 2014). Nevertheless, it is reasonable to assume that smaller planets are more likely to be rocky, and thus we present joint posterior distributions in radius and insolation. An example of this diagram for KOI-0571.05 is given in Figure 13, in which we indicate various boundaries for the HZ as defined by Kopparapu et al. (2013) and Zsom et al. (2013). Similar graphs for the remaining targets in our sample are shown in Figure 14.

From the standpoint of habitability it is of interest also to quantify the likelihood that the planets are rocky, given their measured sizes and corresponding uncertainties. To do this we have considered an empirical density model giving a statistical estimate of the mass of a planet as a function of its radius, constructed based on the available sample of transiting planets with measured densities (i.e., with masses measured either via the Doppler technique, or from TTVs). This model is expected to be biased towards larger and more massive planets that are easier to detect, but it is possible to remove the bias by convolving the density model with estimates of the rate of occurrence of planets as a function of their size (Fressin et al. 2013), which we have done in a Monte Carlo fashion (Fressin et al. 2015). In this way we may infer the true distribution of planets in the mass-radius diagram, which can then be used to establish the fraction of rocky or gaseous planets at a given radius or mass. For the purposes of this work we have considered any planet denser than a composition of 100% MgSiO_3 perovskite to be rocky (Seager et al. 2007). Using the above model and our posterior distributions for the radius of the planets in our sample, we have computed the

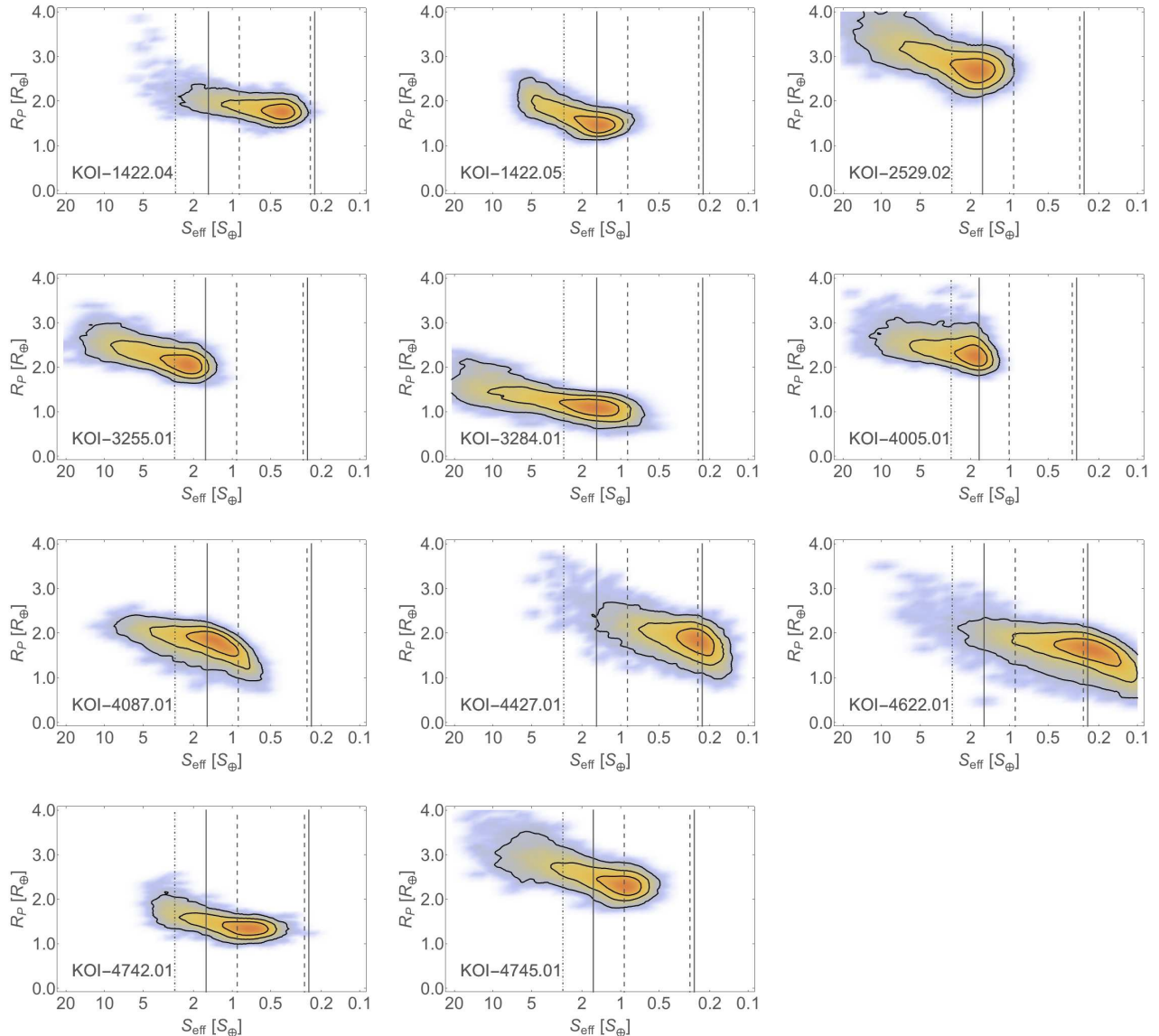


Figure 14. Similar to Fig. 13 for the other planets in this study.

probability that they are rocky, $\mathcal{P}[\text{rocky}]$, by assigning a mass to each link in the chain and counting the number of samples denser than the threshold, analogous to what was done previously for the HZ. The $\mathcal{P}[\text{rocky}]$ values are listed for each object in Tables 8 and 9. Estimates of $\mathcal{P}[\text{rocky}]$ using an alternate density model proposed recently by Rogers (2014) lead to similar assessments, at least qualitatively.

The results of our calculations indicate that all of the planets in our sample have a $\sim 50\%$ or greater chance of being in the temperate region of their parent stars. KOI-0571.05, 1422.04, and 4742.01 are the best candidates for residing within the HZ boundaries, with $\mathcal{P}[\text{HZ}]$ equal to 98.4%, 99.7%, and 96.9%, respectively. The first two receive roughly one third of the flux of the Earth, while the latter receives two thirds. Based on their measured sizes, KOI-0571.05 and KOI-4742.01 have the best chance of being rocky; KOI-1422.04 is larger and has a somewhat smaller chance. KOI-3284.01 is the object in our sample with the highest probability of being rocky

in nature (69.6%); its size is consistent with being the same as that of the Earth: $R_p = 1.12^{+0.16}_{-0.17} R_\oplus$. Other planets with non-negligible chances of being rocky are KOI-1422.05, 4087.01, 4622.01, and 4742.01.³⁰ On the other hand, the larger planets KOI-2529.02, 4005.01, and 4745.01 have $\mathcal{P}[\text{rocky}] \sim 5\%$ or smaller, and are most likely mini-Neptunes. KOI-3255.01 may still be rocky despite its radius of $2.14 R_\oplus$, with $\mathcal{P}[\text{rocky}] = 11.7\%$.

In terms of their insolation, four of our validated planets with a sizable chance of being rocky have S_\oplus values within 50% of that of the Earth: KOI-1422.05, 3284.01, 4087.01, and 4742.01. Of these worlds, KOI-3284.01 and KOI-4742.01 appear to be the most “Earth-like” when considering both their size and amount of incident flux jointly, surpassing KOI-0571.05, which is also rocky but receives only one third of the incident flux of our planet.

³⁰ KOI-4427.01 would otherwise join this group, but it is not formally validated as a planet to the same level as the others. Its insolation is only about a quarter of that of the Earth.

10. DISCUSSION AND CONCLUDING REMARKS

Eleven of the twelve candidates in our sample have been validated here as planets to a very high degree of confidence exceeding 99.73% (3σ). The high bar we have set in this work is commensurate with the importance we assign to these planets, which are all small and potentially in the HZ of their host stars. Few such objects have been verified so far, and our work now essentially doubles the number of cases listed in Sect. 1.

Three of our targets, KOI-0571.05, KOI-1422.04, and KOI-1422.05 are in systems of five planets each, and have been previously validated by others using very different methodologies and assumptions. Our BLENDER validations confirm those assessments using conservative and realistic hypotheses, generally with a higher degree of confidence. KOI-1422.04 and KOI-1422.05 were included in the studies of Lissauer et al. (2014) and Rowe et al. (2014), who considered them to be validated based on the general conclusion that the vast majority ($> 99\%$) of *Kepler* candidates in multiple systems are likely to be bona-fide planets, as they showed statistically.³¹ In the present work we are able to assign a specific confidence level (99.74% and 99.89%) to these two planets using BLENDER. KOI-0571.05 was validated separately by Quintana et al. (2014) through statistical arguments somewhat similar to those in BLENDER in some respects, but not in detail. For example, Quintana et al. (2014) included short period planets in their estimate of the planet prior, whereas we chose to count only planets with similar period as the candidate, because the rates of occurrence of transiting planets are a strong function of orbital period. For a planet with a long period of ~ 130 days such as KOI-0571.05, including short periods overestimates PL by about a factor of 50 according to our calculations. On the other hand, including short periods also for the false positives (both for planets and EBs), as Quintana et al. (2014) have done, will tend to make the blend frequencies higher. This partly offsets the bias from the larger planet prior, but still results in a final odds ratio a factor of 2 greater than if short periods are not included. An additional difference is that in order to reach a comfortable validation level Quintana et al. (2014) applied a “multiplicity boost” to their planet prior (increasing it by a factor of 30), invoking the fact that KOI-0571.05 is in a five-planet system, that the other four planets were considered validated by Lissauer et al. (2014) and Rowe et al. (2014), and that false positives are significantly less common in multis. While this is a perfectly legitimate argument, the odds ratio achieved with BLENDER is high enough (for all our multis) that this boost was not required here. Had we used it, our confidence level for KOI-0571.05 would be 30 times higher.

One of our candidates, KOI-4427.01, does not quite reach our threshold for validation, although in other contexts a 99.16% confidence level such as we achieve might be considered high enough to declare it a bona-fide planet. Interestingly, this is the same candidate for which our centroid motion analysis indicated less confidence than in other cases that the transit signal comes

from the target itself as opposed to a nearby background location, consistent with indications from BLENDER. We note also that the host star does not show a clear rotational signature, which causes its properties to be less well determined than others for which we were able to use an age estimate from gyrochronology to strengthen the model fits. For these reasons we do not include this object among our formally validated planets, although it is entirely possible that additional follow-up observations may enable a higher level of validation in the future. It remains a very interesting object, as it is likely to be within the HZ and also has a fair chance of being rocky.

We find that the mean densities derived photometrically from the individual planets in each of the five-planet systems KOI-0571 and KOI-1422 show very good agreement, supporting the notion (for the first time in KOI-1422) that in each case the five planets orbit the same star. This is further supported by a similar consistency found among the limb-darkening coefficients (u_1 and u_2), which were fitted for separately for each of the planets. For the four targets in our sample with close companions the location of the planets is more uncertain, however. In one case (KOI-2529.02) both BLENDER and AP strongly favor the planet transiting the primary star. For KOI-1422.04, KOI-1422.05, and KOI-3284.01 the evidence is in the same direction but not as strong, and for KOI-3255.01 both BLENDER and AP are inconclusive as to which star has the planet. In these four cases even if the planet orbits the companion the inferred radii are still relatively small ($1.68\text{--}2.25 R_{\oplus}$), and at least for KOI-1422.05 and KOI-3284.01 there is still a good chance they are rocky.

Except for KOI-2529.02, the inferred radii of all our validated planets are nominally smaller than $2.4 R_{\oplus}$. In some cases they are rather different than those reported previously, either because of differences in the stellar radii, or because some of the previous studies have not accounted for dilution by nearby companions. The stellar properties in this work are all based on spectroscopic estimates of the temperature and metallicity, as well as $\log g$ for the hotter stars and other constraints on luminosity for the cooler ones, superseding properties reported previously that have relied only on photometry.

This study has significantly increased the number of small validated transiting planets ($< 2.5 R_{\oplus}$) that are potentially in the HZ of their host star. Excluding those in our sample that have been announced previously, as well as KOI-4427.01, we now add to the list KOI-1422.05(*), KOI-2529.02, KOI-3255.01(*), KOI-3284.01(*), KOI-4005.01, KOI-4087.01(*), KOI-4622(*), KOI-4742.01(*), and KOI-4745.01. The ones followed by an asterisk are small enough to be rocky, with a somewhat reduced chance of that being the case for KOI-3255.01. We note that rather than relying on an estimate of the equilibrium temperature for our assessments regarding the HZ, here we have used the effective insolation, which, as pointed out by Kopparapu et al. (2013), dispenses with the uncertainty in the albedo. Our HZ statements are quantified by providing a probability that the planet lies within the adopted inner and outer edges of the region, which properly accounts for the uncertainties in all measured stellar and planetary properties. Similarly, we have provided a quantitative indication of the probability that each of these planets is rocky, also

³¹ We note that another of our targets, KOI-2529.02, is a candidate in a two-planet system that was also included in the statistical studies above, but it was not considered to be validated there due to unresolved issues with the follow-up observations.

accounting for uncertainties.

A number of the previously announced small HZ planets (see Sect. 1) have radii in excess of $2 R_{\oplus}$, and according to our prescription for \mathcal{P} [rocky] they are significantly less likely to be rocky than perhaps deemed to be the case in the original publications (particularly Kepler-22 b and Kepler-296 f, with radii of $2.38 R_{\oplus}$ and $2.31 R_{\oplus}$, respectively). Thus, with the new examples added here, the list of rocky planets in the HZ is enlarged by a factor of two. KOI-3284.01 and KOI-4742.01 are now the validated, rocky, HZ planets that appear most similar to the Earth when considering both their size ($R_p = 1.12^{+0.16}_{-0.17} R_{\oplus}$ and $R_p = 1.34^{+0.11}_{-0.18} R_{\oplus}$) and insolation ($S_{\text{eff}} = 1.40^{+0.67}_{-0.77} S_{\oplus}$ and $S_{\text{eff}} = 0.66^{+0.23}_{-0.41} S_{\oplus}$) jointly.

We thank the referee for helpful comments on the original manuscript. This paper includes data collected by the *Kepler* spacecraft. Funding for the *Kepler* Mission is provided by NASA's Science Mission Directorate. The research has also made use of the Michael Dodds Computing Facility, of NASA's Astrophysics Data System (ADS), and of data products from the Mikulski Archive for Space Telescopes (MAST). Some of the data presented herein were obtained at the W. M. Keck Observatory, which is operated as a scientific partnership among the California Institute of Technology, the University of California, and NASA. We extend special thanks to those of Hawaiian ancestry on whose sacred mountain of Mauna Kea we are privileged to be guests. GT acknowledges partial support for this work from NASA grant NNX14AB83G (*Kepler* Participating Scientist Program). DMK is supported by the Harvard College Observatory Menzel Fellowship.

REFERENCES

- Adams, E. R., Ciardi, D. R., Dupree, A. K. et al. 2012, *AJ*, 144, 42
- Alibert, Y. 2014, *A&A*, 561, A41
- Ballard, S. et al. 2013, *ApJ*, 773, 98
- Barclay, T., Rowe, J. F., Lissauer, J. J., et al. 2013, *Nature*, 494, 452
- Barnes, J. W., 2007, *PASP*, 119, 986
- Basri, G., Walkowicz, L. M., Batalha, N., et al. 2011, *AJ*, 141, 20
- Batalha, N. M., Rowe, J. F., Bryson, S. T., et al. 2013, *ApJS*, 204, 24
- Brown, T. M., Latham, D. W., Everett, M. E., & Esquerdo, G. A., *AJ*, 142, 112
- Borucki, W. J., Agol, E., Fressin, F. et al. 2013, *Science*, 340, 587
- Borucki, W. J., Koch, D. G., Basri, G., et al. 2011, *ApJ*, 736, 19
- Borucki, W. J., Koch, D. G., Batalha, N., et al. 2012, *ApJ*, 745, 120
- Boyajian, T. S., von Braun, K., van Belle, G., et al. 2013, *ApJ*, 771, 40
- Bryson, S. T., Jenkins, J. M., Gilliland, R. L., et al. 2013, *PASP*, 125, 889
- Bryson, S. T., Tenenbaum, P., Jenkins, J. M., et al. 2010, *ApJ*, 713, L97
- Budding, E. 1977, *Ap&SS*, 48, 207
- Burke, C. J., Bryson, S. T., Mullally, F. et al. 2014, *ApJS*, 210, 19
- Caldwell, D. A., Kolodziejczak, J. J., Van Cleve, J. E., et al. 2010, *ApJ*, 713, L92
- Chabrier, G., Baraffe, I., Allard, G., & Hauschildt, P.-H. 2001, 11th Cambridge Workshop on Cool Stars, Stellar Systems and the Sun, ASP Conf. Ser. 223, eds. R. J. García López, R. Rebolo, and M. R. Zapatero Osorio (San Francisco: ASP), p. 49
- Chubak, C., Marcy, G. W., Fischer, D. A. et al. 2012, arXiv:1207.6212
- Cushing, M. C., Vacca, W. D., & Rayner, J. T. 2004, *PASP*, 116, 362
- Cutri, R. M. et al. 2003, The 2MASS All-Sky Catalog of Point Sources, Univ. of Massachusetts and Infrared Processing and Analysis Center (IPAC/California Institute of Technology)
- Dotter, A., Chaboyer, B., Darko, J., Veselin, K., Baron, E., & Ferguson, J. W. 2008, *ApJS*, 178, 89
- Dressing, C. D., & Charbonneau, D. 2013, *ApJ*, 767, 95
- Dumusque, X., Bonomo, A. S., Haywood, R. D. et al. 2014, *ApJ*, 789, 154
- Epstein, C. R., & Pinsonneault, M. H. 2014, *ApJ*, 780, 159
- Everett, M. E., Howell, S. B., & Kinemuchi, K. 2012, *PASP*, 124, 316
- Feroz, F., Hobson, M. P., & Bridges, M. 2009, *MNRAS*, 398, 1601
- Feroz, F., & Hobson, M. P. 2008, *MNRAS*, 384, 449
- Foreman-Mackey, D., Hogg, D. W., & Morton, T. D. 2014, *ApJ*, 795, 64
- Fressin, F., Torres, G., Rowe, J. F. et al. 2012, *Nature*, 482, 195
- Fressin, F., Torres, G., Charbonneau, D. et al. 2013, *ApJ*, 766, 81
- Fressin, F., Charbonneau, D., & Torres, G. 2015, *ApJ*, submitted
- Gaidos, E. 2013, *ApJ*, 770, 90
- Gilliland, R. L., Cartier, K. M. S., Adams, E. R., Ciardi, D. R., Kalas, P., & Wright, J. T. 2015, *AJ*, 149, 24
- Haywood, M. 1994, *A&A*, 282, 444
- Herter, T. L., Henderson, C. P., Wilson, J. C., et al. 2008, *Proc. SPIE*, 7014,
- Holman, M. J., & Wiegert, P. A. 1999, *AJ*, 117, 621
- Horch, E. P., Gomez, S. C., Sherry, W. H. et al. 2011, *AJ*, 141, 45
- Horch, E. P., Howell, S. B., Everett, M. E., & Ciardi, D. R. 2012, *AJ*, 144, 165
- Horch, E. P., Howell, S. B., Everett, M. E., & Ciardi, D. R. 2014, *ApJ*, 795, 60
- Horch, E. P., Veillette, D. R., Baena Gallé, R. et al. 2009, *AJ*, 137, 5057
- Howard, A. W., Johnson, J. A., Marcy, G. W. et al. 2010, *ApJ*, 721, 1467
- Howell, S. B., Everett, M. E., Sherry, W., Horch, E., & Ciardi, D. R. 2011, *AJ*, 142, 19
- Jenkins, J. M., Caldwell, D. A., & Borucki, W. J. 2002, *ApJ*, 564, 495
- Jenkins, J. M., Caldwell, D. A., Chandrasekaran, H., et al. 2010, *ApJ*, 713, L87
- Johansson, E. M., van Dam, M. A., Stomski, P. J. et al. 2008, *Proc. SPIE*, 7015, 70153E
- Kasting, J. F., Whitmire, D. P., & Reynolds, R. T. 1993, *Icarus*, 101, 108
- Kipping, D. M. 2010, *MNRAS*, 408, 1758
- Kipping, D. M. 2013a, *MNRAS*, 434, L51
- Kipping, D. M. 2013b, *MNRAS*, 435, 2152
- Kipping, D. M. 2014a, *MNRAS*, 440, 2164
- Kipping, D. M. 2014b, *MNRAS*, 444, 2263
- Kipping, D. M., Dunn, W. R., Jasinski, J. M., & Manthri, V. P. 2012, *MNRAS*, 421, 1166
- Kipping, D. M., Nesvorný, D., Buchhave, L. A., et al. 2014a, *ApJ*, 784, 28
- Kipping, D. M., Torres, G., Buchhave, L. A. et al. 2014b, *ApJ*, 795, 25
- Kipping, D. M., Hartman, J., Buchhave, L. A., et al. 2013, *ApJ*, 770, 101
- Kolbl, R., Marcy, G. W., Isaacson, H., & Howard, A. W. 2015, *AJ*, 149, 18
- Kolodziejczak, J. J., Caldwell, D. A., Van Cleve, J. E., et al. 2010, *Proc. SPIE*, 7742,
- Kopparapu, R. K., Ramirez, R., Kasting, J. F., et al. 2013, *ApJ*, 765, 131
- Kopparapu, R. K., Ramirez, R. M., SchottelKotte, J., Kasting, J. F., Domagal-Goldman, S., & Eymet, V. 2014, *ApJ*, 787, 29
- Kundurthy, P., Agol, E., Becker, A. C., et al. 2011, *ApJ*, 731, 123
- Lawrence, A., Warren, S. J., Almaini, O. et al. 2007, *MNRAS*, 379, 1599
- Lecante, J., Forget, F., Charnay, B., Wordsworth, R., & Pottier, A. 2013, *Nature*, 504, 268
- Lissauer, J. J., Marcy, G. W., Bryson, S. T., et al. 2014, *ApJ*, 784, 44
- Lopez, E. D., & Fortney, J. J. 2013, *ApJ*, 792, 1
- Mandel, K., & Agol, E. 2002, *ApJ*, 580, L171

- Mann, A. W., Gaidos, E., Kraus, A., & Hilton, E. J. 2013a, *ApJ*, 770, 43
- Mann, A. W., Gaidos, E., & Ansdell, M. 2013b, *ApJ*, 779, 188
- Mann, A. W., Brewer, J. M., Gaidos, E., Lépine, S., & Hilton, E. J. 2013c, *AJ*, 145, 52
- Marcy, G. W., Isaacson, H., Howard, A. W. et al. 2014, *ApJS*, 210, 20
- McCauliff, S., Jenkins, J. M., Catanzarite, J., et al. 2014, submitted (arXiv:1408.1496)
- McQuillan, A., Aigrain, S., & Mazeh, T. 2013, *MNRAS*, 432, 1203
- Meibom, S., Torres, G., Fressin, F. et al. 2013, *Nature*, 499, 55
- Morton, T. D. 2012, *ApJ*, 761, 6
- Morton, T. D., & Johnson, J. A. 2011, *ApJ*, 738, 170
- Muirhead, P. S., Hamren, K., Schlawin, E., Rojas-Ayala, B., Covey, K. R. & Lloyd, J. P. 2012, *ApJ*, 750, 37
- Muirhead, P. S., Becker, J., Feiden, G. A. et al. 2014, *ApJ*, 213, 5
- Newton, E. R., Charbonneau, D., Irwin, J., et al. 2014a, *AJ*, 147, 20
- Newton, E. R., Charbonneau, D., Irwin, J., & Mann, A. W. 2015, *ApJ*, in press (arXiv:1412.2758)
- Nielsen, M. B., & Karoff, C. 2012, *AN*, 333, 1036
- Nielsen, M. B., Gizon, L., Schunker, H., & Karoff, C. 2013, *A&A*, 557, L10
- Petigura, E. A., Howard, A. W., & Marcy, G. W. 2013, *Proceedings of the National Academy of Science*, 110, 19273
- Pintr, P., Peřinová, V., Lukš, A., & Pathak, A. 2014, *Planet. Space Sci.*, 99, 1
- Quintana, E. V., Barclay, T., Raymond, S. N., et al. 2014, *Science*, 344, 277
- Raghavan, D., McAlister, H. A., Henry, T. J. et al. 2010, *ApJS*, 190, 1
- Reinhold, T., Reiners, A., & Basri, G. 2013, *A&A*, 560, A4
- Robin, A. C., Marshall, D. J., Schultheis, M., & Reylé, C. 2012, *A&A*, 538, A106
- Robin, A. C., Reylé, C., Derrière, S., & Picaud, S. 2003, *A&A*, 409, 523
- Rojas-Ayala, B., Covey, K. R., Muirhead, P. S., & Lloyd, J. P. 2010, *ApJ*, 720, L113
- Rojas-Ayala, B., Covey, K. R., Muirhead, P. S., & Lloyd, J. P. 2012, *ApJ*, 748, 93
- Rogers, L. A. 2014, *ApJ*, submitted (arXiv:1407.4457)
- Rowe, J. F., Bryson, S. T., Marcy, G. W. et al. 2014, *ApJ*, 784, 45
- Santerne, A., Fressin, F., Díaz, R. F., et al. 2013, *A&A*, 557, A139
- Seager, S. 2013, *Science*, 340, 577
- Seager, S., Kuchner, M., Hier-Majumder, C. A., & Militzer, B. 2007, *ApJ*, 669, 1279
- Selsis, F., Kasting, J. F., Levrard, B., et al. 2007, *A&A*, 476, 1373
- Slawson, R. W., Prša, A., Welsh, W. F. et al. 2011, *AJ*, 142, 160
- Smith, J. C., Stumpe, M. C., Van Cleve, J. E., et al. 2012, *PASP*, 124, 1000
- Sozzetti, A., Torres, G., Charbonneau, D., et al. 2007, *ApJ*, 664, 1190
- Star, K. M., Gilliland, R. L., Wright, J. T., & Ciardi, D. R. 2014, *ApJ*, submitted (arXiv:1407.1057)
- Tenenbaum, P., Jenkins, J. M., Seader, S., et al. 2013, *ApJS*, 206, 5
- Terrien, R. C., Mahadevan, S., Bender, C. F., et al. 2012, *ApJ*, 747, L38
- Tingley, B., Bonomo, A. S., & Deeg, H. J. 2011, *ApJ*, 726, 112
- Tokovinin, A. 2014, *AJ*, 147, 87
- Torres, G., Winn, J. N., & Holman, M. J. 2008, *ApJ*, 677, 1324
- Torres, G., Konacki, M., Sasselov, D. D., & Jha, S. 2004, *ApJ*, 614, 979
- Torres, G., Fressin, F., Batalha, N. M. et al. 2011, *ApJ*, 727, 24
- Vogt, S. S., Allen, S. L., Bigelow, B. C. et al. 1994, *Proc. SPIE*, 2198, 362
- Waldmann, I. P. 2012, *ApJ*, 747, 12
- Wang, J., Xie, J.-W., Barclay, T., & Fischer, D. A. 2014, *ApJ*, 783, 4
- Weiss, L. M., & Marcy, G. W. 2014, *ApJ*, 783, L6
- Weiss, L. M., Marcy, G. W., Rowe, J. F., et al. 2013, *ApJ*, 768, 14
- Wizinowich, P. L., Le Mignant, D., Bouchez, A. et al. 2004, *Proc. SPIE*, 5490, 1
- Wolfgang, A., & Lopez, E. 2014, *ApJ*, submitted (arXiv:1409.2982)
- Wu, H., Twicken, J. D., Tenenbaum, P., et al. 2010, *Proc. SPIE*, 7740,
- Zsom, A., Seager, S., de Wit, J., & Stamenković, V. 2013, *ApJ*, 778, 109